Timing and Origin of Compressional Tectonism in Mare Tranquillitatis

Enter authors here: T. Frueh[1], H. Hiesinger[1], C. van der Bogert[1], J. Clark[2], T. R. Watters[3], and N. Schmedemann[1]

[1] Institut für Planetologie, Westfälische Wilhelms-Universität Münster, Wilhelm-Klemm-Str.10, 48149 Münster, Germany.

[2] School of Earth and Space Exploration, Arizona State University, 3603 Tempe, AZ, USA.

[3] Center of Earth and Planetary Studies, National Air and Space Museum, Smithsonian Institution, 37012 Washington, DC, USA.

Corresponding author: Thomas Frueh (thomas.frueh@uni-muenster.de)

Key Points:

- Early compressional tectonism in Tranquillitatis, in the form of wrinkle ridges, is presumably related to subsidence and basin loading.
- Later tectonism could reflect the evolution from a basin-localized to a global stress field and the continued growth of ancient faults.
- Recent wrinkle ridge and lobate scarp formation in Tranquillitatis occurred in the last 50 Ma and is influenced by a global stress field.

Abstract

The lithosphere of the Moon has been deformed by tectonic processes for at least 4 billion years, resulting in a variety of tectonic surface features. Extensional large lunar graben formed during an early phase of net thermal expansion before 3.6 Ga. With the emplacement of mare basalts at ~3.9 – 4.0 Ga, faulting and folding of the mare basalts initiated, and wrinkle ridges formed. Lunar wrinkle ridges exclusively occur within the lunar maria and are thought to be the result of superisostatic loading by dense mare basalts. Since 3.6 Ga, the Moon is in a thermal state of net contraction, which led to the global formation of small lobate thrust faults called lobate scarps. Hence, lunar tectonism recorded changes in the global and regional stress fields and is, therefore, an important archive for the thermal evolution of the Moon. Here, we mapped tectonic features in the non-mascon basin Mare Tranquillitatis and classified these features according to their respective erosional states. This classification aims to give new insights into the timing of lunar tectonism and the associated stress fields. We found a wide time range of tectonic activity, ranging from ancient to recent (3.8 Ga to < 50 Ma). Early wrinkle ridge formation seems to be closely related to subsidence and flexure. For the recent and ongoing growth of wrinkle ridges and lobate scarps, global contraction with a combination of recession stresses, diurnal tidal stresses, as well as with a combination of SPA ejecta loading and true polar wander are likely.

Plain Language Summary

The lithosphere of the Moon has been deformed by tectonic processes for at least 4 billion years, resulting in a variety of tectonic surface features. Simple compressional asymmetric landforms are called lobate scarps and complex compressional features, which form as a result of the combination of faulting and folding, are known as wrinkle ridges. Lunar wrinkle ridges only occur within the lunar maria. It has been argued that their formation is linked to the subsidence of the dense mare basalts, which would have happened in the early history of the Moon. We mapped all of these features within one dark lunar region called Mare Tranquillitatis and then studied their morphology on high-resolution images. Based on their morphology, we found a wide time range of tectonic activity, ranging from ancient to recent. Large wrinkle ridges seem to be ancient and influenced by subsidence. Smaller wrinkle ridges and lobate scarps show signs of recent activity. They likely formed recently within the last hundred million years because of the Moon's current state of global compression.

1 Introduction

The Moon's surface hosts a variety of extensional and compressional tectonic features, which recorded the history of the acting regional and global stress systems. Compressional tectonism was initiated with the emplacement of the mare basalts and the shift of net global extension to net global contract at ~3.6 Ga, which led to the formation of the two major compressional tectonic landforms: lobate scarps and wrinkle ridges (Fagin et al., 1978; Lucchitta & Watkins, 1978; Solomon & Head, 1979; Wilhelms, 1987; Watters et al., 2009). Lobate scarps are the surface expressions of simple thrust faults and are the dominating tectonic landforms in the lunar highlands (Binder & Gunga, 1985; Watters et al., 2009, 2010). Lunar wrinkle ridges exclusively occur in the maria or basalt-covered regions and are a result of a complex interaction between thrust faulting and folding (Lucchitta, 1976; Wilhelms, 1987; Schultz, 2000; Watters et al., 2009). The compressional tectonism in the maria is thought to have originated from the superisostatic loading by dense mare basalts and the flexure of the lithosphere (Freed et al., 2001). This model has been established for the mascon (mass concentrations) maria, like Mare Imbrium or Mare Serenitatis. However, not all lunar maria are considered to be mascons because they lack the strong positive gravitational signal of mascon basins (Muller and Sjogren, 1968). The stress systems of those non-mascon basins are less well understood and still a matter of discussion.

Furthermore, the acting stress fields changed with time, and the age of tectonic landforms, therefore, contains important information on the stresses triggering their formation. Most of the deformation of the maria is thought to have occurred early in lunar history (e.g., Fagin et al., 1978; Ono et al., 2009; Watters et al., 2009; Yue et al., 2017). However, recent studies uncovered young tectonic features in the lunar highlands and maria, including young and recently active wrinkle ridges (e.g., Watters et al., 2010; Williams et al., 2019; Lu et al., 2019; Valantinas & Schultz, 2020; Nypaver & Thomson, 2022). The young landforms exhibit distinctive morphological features, like steep slopes, sharp edges, a crisp appearance, crosscutting relationships with craters, and the occurrence of small crisp graben in their close vicinity (Fig. 1). The trigger behind this recent tectonic activity is, also, still a matter of discussion.

Mare Tranquillitatis, which was the stage of the first human landing site as part of the Apollo 11 mission, is one of those non-mascon basins. Mare Tranquillitatis is an irregularly-shaped basin (Fig. 2), consisting of a deep and deeply basalt-filled western part and a shallow and shallow-filled eastern part (Dvorak & Phillips, 1979; De Hon, 1974, 2017; Konopliv et al., 2001; Zuber et al., 2013). The western part is associated with intensive deformation and circular, radial, and NS trending wrinkle ridge patterns, while the eastern part experienced less deformation and exhibits loose wrinkle ridge patterns. In addition to wrinkle ridges, lobate scarps, graben, and a large normal fault (called Rupes Cauchy) are present in the mare. A study by Yue et al. (2017), discovered an unusually young average age of ~2.4 Ga of large wrinkle ridges in Mare Tranquillitatis relative to wrinkle ridges in other maria. The reason behind this discrepancy remains unknown.

This study aims to contribute to the discussion on the age of tectonic landforms, stress systems of non-mascon maria, and the trigger behind recent tectonic activity. To achieve this goal, we created a tectonic map of Mare Tranquillitatis and studied the degradational state of compressional tectonic features to gain age information. By combining the tectonic analysis with

the age of the tectonic features, we aim to uncover the evolution of the stress field acting in Mare Tranquillitatis.

2 Background

2.1 Lunar Tectonics

The tectonic history of the Moon began with a period of net thermal expansion, which is argued to have shifted to net contraction around 3.6 Ga (Lucchitta & Watkins, 1978). Since then, global cooling induced a dominantly contractional global stress field (Solomon & Head, 1979; Wilhelms, 1987; Watters et al., 2009). This shift in the thermal state of the Moon is preserved in its tectonic landforms. Large scale crustal extension and, thus, the formation of large lunar graben ended at ~3.6 Ga (Lucchitta & Watkins, 1978; Watters et al., 2009). Following the shift, compressional features, i.e., lobate scarps, became the dominant globally forming tectonic landforms. The emplacement of the mare basalts started at ~3.9 – ~4.0 Ga and generally ceased at ~1.2 Ga (Hiesinger et al., 2011). With the main period of basalt emplacement at about 3.6 – 3.8 Ga (Hiesinger et al., 2011), the formation of wrinkle ridges began (Fagin et al., 1978; Watters, 1988; Watters et al., 2009).

Wrinkle ridges are common contractional tectonic features on the Moon, Mercury, Mars, and Venus (Plescia & Golombek, 1986; Watters, 1988; Golombek et al., 1991; Watters et al., 2009). On the Moon, wrinkle ridges exclusively occur within the mare basins (Lucchitta, 1976; Wilhelms, 1987; Watters et al., 2009), to which they typically appear radial and concentric (Whitaker, 1981; Watters et al., 2009). They typically show an asymmetric profile and consist of a broad arch and a superimposed irregular ridge (Plescia & Golombek, 1986; Strom, 1972; Watters, 1988), but their morphology is highly variable (Plescia & Golombek, 1986; Watters, 1988). Wrinkle ridges reach up to 300 km in length and 20 km in width (Sharpton & Head, 1988). Often one flank of the wrinkle ridge, the vergent side, has a steeper slope than the other, but this asymmetry can reverse along the wrinkle ridge. The superposed ridge usually is located near the steeper flank of the arch (Plescia & Golombek, 1986; Watters, 1988). However, both structures can occur independently from one another (Watters et al., 2009). Wrinkle ridge segments often occur in en-echelon arrangements (Watters et al., 2009). Smaller secondary or tertiary ridges occur near or on top of larger primary ridges (Watters, 1988; Watters et al., 2009). The surface texture of wrinkle ridges often resembles a crisscross “elephant-hide” structure (Gold, 1972). Elephant-hide structure can be found on slopes everywhere on the Moon and is thought to form due to regolith creep and seismic shaking (Zharkova et al., 2020; Bondarenko et al., 2022).

Since wrinkle ridges deform even young mare basalts with an age of ~1.2 Ga, crustal shortening associated with lunar maria occurred at least as recently as ~1.2 Ga (Watters et al., 2009). A global survey of possible formation times found average ages > 3.0 Ga for large wrinkle ridge structures (Yue et al., 2017). Wrinkle ridges in Mare Tranquillitatis, however, appear to be younger with an average age of ~2.4 Ga (Yue et al., 2017; McGovern et al., 2022).

While the exact kinematics of wrinkle ridge formation are still debated, the formation is generally explained by a combination of thrusting and folding (Schultz, 2000; Watters et al., 2009). Hence, wrinkle ridges can be interpreted as anticlinal structures above a non-surface breaking blind thrust fault (Schultz, 2000; Watters et al., 2009). For these processes to occur, a layered stratigraphy of the mare basalts is necessary (Schultz, 2000). The fault geometry may be

planar or listric, there may be a single or multiple faults, and the depth of faulting may be shallow or deep (i.e., thick- or thin-skinned deformation; Schultz, 2000; Montési & Zuber, 2003; Okubo & Schultz, 2003, 2004; Watters, 2004, 2022). Wrinkle ridge formation is thought to be the result of superisostatic loading by dense mare basalts inducing subsidence and flexure of the lithosphere (i.e., mascon tectonics; Freed et al., 2001; Byrne et al., 2015; Schleicher et al., 2019). This led to compressional stresses in the basin center and extensional stresses at the basin margins, and, consequently, in basin concentric and radial wrinkle ridges (Freed et al., 2001). It is also suggested that global cooling instead of subsidence was the dominant cause of wrinkle ridge formation after 3.55 Ga onwards (Ono et al., 2009; Watters et al., 2009). Another proposed influence on the global stress field and wrinkle formation is deep transient stresses generated by the South Pole-Aitken (SPA) basin (Schultz & Crawford, 2011). This model predicts antipodal failures on the lunar nearside due to extensions deep within the Moon, which would have reactivated deep-seated faults. Wrinkle ridge patterns of the lunar nearside do spatially correlate with wrinkle ridge patterns predicted by this model (Schultz & Crawford, 2011; Valantinas & Schultz, 2020). GRAIL Bouguer gravity gradient data revealed a possible quasi-rectangular pattern of ancient deep rift valleys that are proposed to influence the localization of some wrinkle ridges (Fig.2; Andrews-Hanna et al., 2014). Wrinkle ridge formation might, therefore, be a result of an interplay of various factors on the regional and global stress fields, which will be discussed later.

Lobate scarps are linear to curvilinear small-scaled compressional structures, which mainly occur in the lunar highlands. They are asymmetric with a steeply sloping scarp face and gently sloping back scarp. The scarp face's direction often reverses along the strike (Binder & Gunga, 1985; Watters et al., 2009, 2010). In contrast to wrinkle ridges, they are thought to result from shallow surface-breaking thrust faults (Watters et al., 2009). In some cases, wrinkle ridges transform into lobate scarps at mare highland boundaries (Lucchitta, 1976; Watters et al., 2009, 2010; Clark et al., 2019). Lobate scarps are thought to be among the youngest tectonic features on the Moon (e.g., Binder & Gunga, 1985; van der Bogert et al., 2018; Watters et al., 2009, 2010, 2019). Binder and Gunga (1985) suggested that highland scarps are younger than 1 Ga. Crater size-frequency distribution (CSFD) measurements of lobate scarps support late Copernican ages (van der Bogert et al., 2018). From infilling rates of small-scale back-scarp graben, the age of the lobate scarps is likely < 50 Ma (Watters et al., 2012).

Recent studies revealed fresh activity of wrinkle ridges and lobate scarps (e.g., Watters et al., 2010; Williams et al., 2019; Lu et al., 2019; Valantinas & Schultz, 2020; Nypaver & Thomson, 2022). The evidence includes for both landforms (Fig. 1), the abundance of boulder fields and patches (French et al., 2019; Watters et al., 2019; Valantinas & Schultz, 2020), a distinct crisp morphology (e.g., Watters et al., 2010; Williams et al., 2019), crosscutting of impact craters (Watters et al., 2010; Lu et al., 2019; Nypaver & Thomson, 2022), ages <1 Ga determined from CSFD methods (van der Bogert et al., 2018; Valantinas et al., 2018; Lu et al., 2019), shallow moonquakes (Watters et al., 2019), boulder falls (Kumar et al., 2016), and associated small meter-scaled graben (Fig. 3; Watters et al., 2012; French et al., 2015; Valantinas & Schultz, 2020). The correlation between boulder falls and seismic activity, however, has been questioned lately (Bickel et al., 2021; Ikeda et al., 2022), highlighting the ongoing and early state of the study of recent tectonic activity. Late-stage global contraction is consistent with both an initially molten Moon (Binder & Gunga, 1985; Watters et al., 2019) and a near-surface magma ocean (Solomon, 1986; Solomon & Head, 1979; Watters et al., 2019), however, the magnitude of the late-stage stresses predicted in the totally molten Moon model is inconsistent with the

184 population of small lobate thrust fault scarps (Watters et al., 2012, 2015). Global contraction
185 would result in scarps with random orientations (Watters et al., 2015, 2019). However, since
186 scarp orientations are non-randomly distributed, Watters et al. (2015, 2019) proposed a
187 significant contribution of tidal stresses in the current stress state on the Moon. These stresses
188 might also be an important influence on recent wrinkle ridge formation and activity (Williams et
189 al., 2019). A model including South Pole-Aitken ejecta loading, true polar wander, and global
190 contraction is also able to reproduce the observed scarp distribution (Matsuyama et al., 2021).
191 Valantinas and Schultz (2020) proposed that active wrinkle ridges are part of an active nearside
192 tectonic system (ANTS), resulting from the fault adjustment of ancient deep-seated intrusions,
193 which were reactivated by the SPA forming impact. Deep moonquakes could be possible signs
194 of those readjustments (Valantinas & Schultz, 2020). However, stresses related to these ancient
195 sources of activity may have largely relaxed long ago and further models are needed to quantify
196 their influence on today's global stress field.

197

198 2.2 Mare Tranquillitatis

199 Mare Tranquillitatis is centered at 8.35°N, 30.83°E, and extends over approximately 875
200 km in diameter (Fig. 2). In the northwest, it borders Mare Serenitatis and Mare Fecunditatis in
201 the southeast. Mare Tranquillitatis is irregularly shaped and dividable into two regions. The
202 eastern part has a higher topographic elevation of up to –350 m (Fig 2). The western region has a
203 lower elevation of below –2,000 km. The somewhat irregular shape of Tranquillitatis does not
204 resemble the typical circular mare basin shape (e.g., Mare Imbrium, Mare Serenitatis, or Mare
205 Crisium).

206 Mare Tranquillitatis is a non-mascon basin of pre-Nectarian age (Wilhelms et al., 1987).
207 The mare fills at least one multi-ring basin (De Hon, 1974; Spudis, 1993), but a second
208 overlapping basin is possible (De Hon, 2017; Bhatt et al., 2020). The mare basalts of Mare
209 Tranquillitatis are of Imbrian age of 3.39 – 4.23 Ga (Hiesinger et al., 2000; Hiesinger et al.,
210 2011). Most of the basalts show a CSFD age of 3.6 – 3.7 Ga (Hiesinger et al., 2000). These ages
211 agree with the radiometric age of 3.67 Ga of the returned Apollo 11 samples (Wilhelms et al.,
212 1987; Hiesinger et al., 2000; Iqbal et al., 2019). The western part of Mare Tranquillitatis is
213 slightly younger than the eastern part (Hiesinger et al., 2000; Hiesinger et al., 2011). Crustal
214 thickness varies from west to east as well. With a thickness between 10 and 30 km, the crust is
215 thinnest in the west. This agrees with the free air data, which indicate a positive gravity anomaly
216 in the western region (Fig. 2; Zuber et al., 2013). This gravitational anomaly suggests a trough-
217 like structure connecting Mare Tranquillitatis with Mare Nectaris in the south and Mare
218 Serenitatis in the north (De Hon, 1974). Recent publications suggest that this trough is part of a
219 system of deep-seated intrusions that form a rectangular pattern on the near side of the Moon
220 (Andrews-Hanna et al., 2014; Valantinas & Schultz, 2020). The deepest basalt-filled regions of
221 the trough in Mare Tranquillitatis are the Lamont region and a structure near Torricelli crater
222 (Dvorak & Phillips, 1979; De Hon, 1974, 2017; Konopliv et al., 2001; Zuber et al., 2013). The
223 Lamont region represents a circular positive free air anomaly in the southwest of Tranquillitatis
224 and is superficially recognizable as a circular ring of wrinkle ridges and an overall topographic
225 low (Dvorak & Phillips, 1979; Scott, 1974). It has been interpreted to be either a buried impact
226 crater or ghost crater (Dvorak & Phillips, 1979; Scott, 1974) or a feature of volcanic origin
227 (Zhang et al., 2018). Several large graben occur throughout the mare, but most of them in the
228 western region of Mare Tranquillitatis. The large graben Rima Cauchy and a parallel normal

fault called Rupes Cauchy occur in eastern Mare Tranquillitatis (Bhatt et al., 2020). Many smaller volcanic domes and cones are abundant in the eastern mare (Spudis et al., 2013; Qiao et al., 2020). Spudis et al. (2013) proposed two large shield volcano-like structures in eastern Mare Tranquillitatis as an explanation for the abundance of volcanic features. Mare Tranquillitatis has the largest abundance of irregular mare patches, which were interpreted to be evidence of volcanism within the past 100 Ma (Braden et al., 2014; Qiao et al., 2020).

2 Data and Methods

In this study, a tectonic map and a tectonic feature map of Mare Tranquillitatis and the adjacent highlands were created using ESRI's ArcGIS version 10.5.1 and ArcGIS Pro. Wrinkle ridges and lobate scarps typically consist of a variable number of individual segments. In the tectonic map, e.g., a wrinkle ridge consisting of several individual segments is represented by one continuous polyline. This map was used for the tectonic analysis. For the feature map, we mapped the individual segments for morphological analysis, because individual segments might have varying formation ages. Both maps were created on Kaguya TC images (pixel scale of ~10 m; Ohtake et al., 2008) at a scale of 1:80,000. To achieve complete coverage of Mare Tranquillitatis, 84 TC tiles of both west and east illumination maps were integrated into the ArcGIS environment. Topographic information was gathered from the merged LRO LOLA – SELENE Kaguya DEM (Barker et al., 2016). Hillshade maps with different azimuth and height combinations, as well as slope maps were derived from this DEM.

For the tectonic map, features were classified as wrinkle ridges, lobate scarps, and unidentified. Unidentified features are linear positive topographic features with a possible but unproven tectonic origin (other possible origins are, e.g., dikes, lava flows, surface expressions of buried structures, or ejecta remnants). Additionally, we mapped extensional features, i.e., graben and the normal fault segments of Rupes Cauchy for complete coverage of the tectonic setting of Mare Tranquillitatis and for the following tectonic analysis. The polylines of wrinkle ridges were drawn at the center of the anticline. Since the morphology of wrinkle ridges is highly variable, Kaguya TC images, topographical data, slope maps, and hillshade maps were used to identify wrinkle ridge structures. A wrinkle ridge was mapped if it exhibits the classical morphological characteristics (as described in section 2.1) or shows a distinguishable asymmetric change in slope and topography. For lobate scarps and normal faults, the polylines were drawn at the scarp face base and for graben, the polylines were drawn at the graben center.

For the feature map, we focused on Kaguya TC images to identify individual features of wrinkle ridges and lobate scarps. Polylines were drawn on top of each wrinkle ridge crest. Every polyline represents a continuous wrinkle ridge crest segment. A new polyline was drawn if the orientation of the wrinkle ridge changes or if the crest segment is interrupted. Since mapping took place on the 1:80,000 scale, smaller structures are mostly represented by a single polyline. If no crest could be visibly identified, the edge of the steeper side was used for mapping. Lobate scarps features were mapped at the scarp face base. The morphology of each of these mapped features was then examined on NAC images in Quickmap and ArcGIS, with incidence angles of between 55° and 90°. Each wrinkle ridge segment was classified according to their respective appearances and erosional states into the classes crisp, moderately degraded, advanced degraded, and heavily degraded (similar to Williams et al., 2019). Attention was paid to their general appearance, the number of crosscut and superimposed craters, and to small associated graben (Table 1). The boulder abundance was not used in the classification, because we want to compare our results to previously published boulder abundance maps (French et al., 2019; Valantinas & Schultz, 2020).

278

279

280

281

282 Table 1

283 *Characteristics Used for the Classification of the Erosional States of Wrinkle Ridges and*
284 *Lobate Scarps*

285

Class	Morphology	Crater crosscutting	Graben
Crisp	Features with sharp and morphologically distinct edges and steep slopes.	Can crosscut and deform craters with diameter ranges of < 50 – 100 m.	Small (width < 50 m) and crisp clusters of graben are present.
Moderately Degraded	Features with slightly rounded edges and steep to moderate slopes.	Can crosscut and deform craters with, generally, ≥ 100 m in diameter.	Generally, not associated with small graben. Rarely, diffusive troughs can be associated with features of this class.
Advanced Degraded	Features with moderate to gentle slopes and well-rounded edges.	Rarely deform and crosscut craters with diameters of several kilometers.	No small graben associated with those features.
Heavily Degraded	Features with gentle slopes and often indistinctive morphologies, not following the standard wrinkle morphology described in section 2.1.	Generally, do not crosscut superimposed craters.	No small graben associated with those features.

286

287 *Note*. Slopes and morphological descriptions are described relative to each other.

3 Results

A total of 242 wrinkle ridges, 137 lobate scarps, and 148 unidentified structures, with a total length of ~10,991 km, were mapped in this study (Fig. 3). The length of individual segments ranges from ~1 km to ~175 km, with a mean length of ~21 km. The mapped wrinkle ridges have a total length of ~7,852 km and range from ~3.7 km to ~175 km. The wrinkle ridge mean length is 32.8 km. Lobate scarps have a total length of ~946.4 km with a minimum length of ~1 km and a maximum length of ~58.5 km. The lobate scarp mean length is ~7 km.

The differences in the appearance of the ridge segments allow distinguishing four different classes. These classes are crisp, moderately degraded, advanced degraded, and heavily degraded. They differ from one another in their erosional state, general structure, surface texture, crosscut relationships, and small graben occurrence. However, transitions between the different degradation classes are gradual. A total of 846 segments of contractional tectonic features were mapped of which 658 segments were classified (Fig. 4). Their appearances and occurrences are described in the following.

A total of 49 segments with a cumulative length of ~451 km and an average length of ~9.2 km were classified as crisp (Fig. 5). Consequently, they represent 5.1% of the total mapped length. Crisp features consist of wrinkle ridges and lobate scarps. All of them occur scattered within Mare Tranquillitatis and are often close to moderately degraded features (Fig. 4). In general, they have a NW – WNW orientation. Crisp features have sharp edges, and steep slopes on a small scale (< 100 m; Fig. 5). They are generally relatively small structures in terms of length and width and have a winding and lobate appearance. They often braid and cross each other along strike. The crisp wrinkle ridges often resemble a lobate scarp morphology, with a simple asymmetrical profile and, in some cases, a seemingly missing broad arch. Often smaller surface-breaking tectonic features occur in their vicinity. Crisp features, generally, crosscut small craters (Fig. 5c; < 50 – 100 m diameter) and wrinkle ridges often appear to be surface breaking when they crosscut craters. Clusters of small (width < 50 m) crisp appearing graben and troughs are present on top of and in the close vicinity of crisp features (Fig. 5). Generally, the graben are located at the hanging wall and are oriented perpendicular and parallel to the latter. Small boulder patches are visible occasionally (Fig. 5b).

About 100 segments were classified as moderately degraded (Fig. 6). They have a total length of ~780 km, which makes up 8.9% of the total mapped length. On average, they have a ~7.8 km length and generally show a NW orientation. Moderately degraded features are comprised of lobate scarps and wrinkle ridges. The structures are similar in size to the crisp segments, but the edges can be more indistinct than crisp features. In general, they have a winding and lobe-like morphology, and they often braid and cross each other. Only a few small craters superimpose the segments. They typically crosscut several craters along their length, which mostly have diameters of larger than 100 m (Fig. 6). Small graben are generally not associated with these structures. They occur throughout Mare Tranquillitatis and can be spatially associated with crisp, advanced, and heavily degraded features.

Advanced degraded features (Fig. 7) are the second most common class and are dominantly comprised of wrinkle ridges. A total of 251 advanced degraded wrinkle ridges with an average length of ~11 km have been mapped, resulting in a total length of ~2,762 km. This class represents 31.5% of the total length. They are generally the most massive wrinkle ridges

with respect to width and topography (up to 10s of kilometers wide and hundreds of meters high). Their rounded morphology mostly resembles the traditional wrinkle ridge definition, with a, in some cases km scaled, broad arch and an asymmetric superimposed steep crest (Fig. 7a). The changes in the orientation of the wrinkle ridge asymmetry are either gradual or abrupt. Smaller ridge segments of higher order occur in front or back and on the top of these wrinkle ridges. Structures of higher order can transition to first-order ridges along their strike. On slope maps, advanced degraded wrinkle ridges show slopes up to > 30°. They have a larger number of superimposed craters than the previously described morphological classes. However, the abundance of superimposed craters is often lower than crater abundances in the surrounding mare units. These wrinkle ridges can deform and crosscut craters with diameters of several hundred meters, but most segments do not crosscut any craters. The surfaces often show a crisscross pattern that previous studies described as an "elephant-hide" pattern (Fig. 7b; Gold, 1972; Zharkova et al., 2020; Bondarenko et al., 2022). Extensive boulder fields are associated with some advanced degraded wrinkle ridges (Fig. 7).

The most common class are the heavily degraded features (Fig. 8), which also dominantly consist of wrinkle ridges. 258 segments, with a total length of ~3,140 km and an average length of ~12.1 km, were mapped. As a result, 35.8% of the total length is represented by this class. While their overall structure can be similar to advanced degraded wrinkle ridges, they generally have an indistinctive and diffuse morphology with more rounded edges (Fig. 8), and the classical wrinkle ridge structure is often only visible in topographic data. They have many superimposed craters and generally do not crosscut any craters, but rarely can deform craters with diameters of several hundred meters. There are no associated small graben present. Their surface texture can resemble an elephant-hide structure. In general, advanced and heavily degraded wrinkle ridges are similarly distributed. However, individual wrinkle ridge assemblages are generally represented mainly by one of both classes. In general, heavily degraded wrinkle ridges occur less commonly together with crisp and moderately degraded wrinkle ridges than advanced degraded wrinkle ridges. Both classes represent the largest wrinkle ridge structures in Mare Tranquillitatis in length, width, and height.

4 Discussion

The sharp-edged morphology and the relatively small size of the crisp wrinkle ridges and lobate scarps suggest a relatively young formation age in contrast to advanced degraded and heavily degraded features. Crisp features can crosscut craters with diameters of less than 50 - 100 m. Craters of these sizes are estimated to be of Copernican ages (< 800 Ma; Wilhelms et al., 1987), because older craters of this size would have been infilled and degraded since then (Trask, 1971; Basilevsky, 1976; Fassett & Thomson, 2014). Thus, it is possible to establish a Copernican age, i.e., an upper age limit of ~800 Ma for these landforms. Since tectonic activity would result in seismic shaking and thus in enhanced degradation of the small craters, the upper limit is presumably overestimated (Williams et al., 2019). CSFD measurements also support Copernican ages for lobate scarps with similar crisp morphologies (van der Bogert et al., 2018; Clark et al., 2017) and possibly even wrinkle ridges (Valantinas et al., 2018). Accompanying crisp features are small fresh graben and troughs (Fig. 5). The existence of small crisp graben situated near lobate scarps was first documented at the back-limb of the Lee-Lincoln scarp, close to the Apollo 17 landing side (Watters et al., 2010). Since then, more of these structures were found in the

vicinity of lobate scarps (French et al., 2015; Watters et al., 2012) and wrinkle ridges (French et al., 2015; Williams et al., 2019). Small graben observed in Mare Tranquillitatis are similar in their dimensions to the graben described in the latter studies. They typically have widths of less than 50 m and, in many cases, of even less than 10 m. Because of their similarity to sizes measured in other studies, depths of ~17 m to ~1 m can be assumed (Watters et al., 2012; Williams et al., 2019). Fill rates of shallow depressions in lunar regolith are estimated to be 5 ± 3 cm/Ma (Arvidson et al., 1975). Therefore, a ~1 m deep graben should be filled entirely with regolith after ~12.5 to ~50 million years, which implies formation ages of less than 50 Ma. Due to their association with lobate scarps, Watters et al. (2012) suggested that these graben form by uplift and flexural bending resulting from the movement at the underlying thrust fault. Thus, these graben can be viewed as possible evidence for tectonic activity of crisp features during the last 50 Ma (French et al., 2015; Watters et al., 2012; Williams et al., 2019). Lu et al. (2019), used ejecta boulders of craters crosscut by small wrinkle ridges in Mare Imbrium to calculate the individual crater ages since boulder abundances decrease with exposure time (Basilevsky et al., 2013; Ghent et al., 2014; Lu et al., 2019). The derived ages support wrinkle ridge formation during the last 10s of Ma (Lu et al., 2019). The morphology of the young wrinkle ridges studied by Lu et al. (2019) are indistinguishable from crisp wrinkle ridges in Mare Tranquillitatis. In summary, different methods indicate the formation of young wrinkle ridges and lobate scarps on the Moon during the last few 10 to 100 Ma. Thus, we propose tectonic activity for crisp wrinkle ridges and lobate scarps in Mare Tranquillitatis at least during the last 50 Ma, which further highlights the global recent wrinkle ridge formation.

Based on our study we cannot conclusively estimate formation ages for moderately degraded features. Crater crosscutting relationships imply younger ages for moderately degraded wrinkle ridges and lobate scarps than advanced degraded features. The main difference between moderately degraded and crisp features, next to a more rounded morphology, is the apparent lack of small graben. However, while small graben can be seen as possible evidence for recent tectonic activity, it is unknown whether they necessarily have to form during recent activity. Therefore, the lack of crisp graben does not necessarily imply an older age. Furthermore, because of the small size and faint appearance of these graben, as well as the missing NAC coverage (incidence angles between 55° and 90°) of some features, a wider distribution of undetected graben is possible. We estimate that moderately degraded wrinkle ridges and lobate scarps have a broad range of formation ages in between crisp and advanced degraded features.

Crisp features occur scattered within Mare Tranquillitatis and do not align with patterns predicted by basin loading and subsidence. Hence, subsidence does not seem to be the major controlling factor of young wrinkle ridge and lobate scarp formation. Additionally, they are not correlated with positive gravitational anomalies within the mare (Fig. 9, 10). However, as previously stated, Mare Tranquillitatis is of irregular shape, which could influence subsidence-induced stress patterns, and the role of the thickness of the elastic lithosphere in wrinkle ridge formation is also a factor (Watters, 2022). Previous studies discussed the prolonged cooling, triggered by the abundance of heat-producing elements, of the Procellarum KREEP Terrane (PKT) to be a factor in recent wrinkle ridge formation (Daket et al., 2016; Lu et al., 2019). However, Mare Tranquillitatis is not associated with the PKT (Wieczorek & Phillips, 2000). Therefore, this model does also not explain the recent formation of wrinkle ridges and lobate scarps in Mare Tranquillitatis. Late-stage global compressional stresses are consistent with both an initially completely molten Moon and an initially hot exterior and magma ocean (Binder & Gunga, 1985; Solomon & Head, 1979; Watters et al., 2019; Williams et al., 2013). The interior

cooling of the Moon could result in compressional stresses of ≥ 2, but < 10 MPa (Watters et al., 2015, 2019). For shallow thrust faults to form, an estimated ~2 - 7 MPa are sufficient (Watters et al., 2019; Williams et al., 2013). Small-scale wrinkle ridges were likely formed by shallow thrust faults (Lu et al., 2019; Watters, 2004). The derived depths from Lu et al. (2019) for small wrinkle ridge thrust faults are similar to suggested depths of shallow lobate scarps (~1 km; Williams et al., 2013). Concluding, global compression seems to be a likely candidate as the driving force behind recent wrinkle ridge and lobate scarp formation on the Moon and in Mare Tranquillitatis. Global lobate scarp patterns and the timing of detected moonquakes highlighted the possible influence of tidal forces, such as orbital recession, diurnal tidal stresses, and true polar wander onto the lunar stress field (Matsuyama et al., 2021; Watters et al., 2019). Models of an additional influence of SPA ejecta loading onto the global stress field also showed good fitting results and are discussed as an alternative or addition to the influence of tidal forces (Matsuyama et al., 2021). N to NW orientated faults between ~20°E and ~40°E, and ~0°N to ~20°N are predicted by a combination of recession stresses, diurnal tidal stresses at apogee, and global contraction (Watters et al., 2015, 2019), as well as by a combination of SPA loading, true polar wander, and global contraction (Matsuyama et al., 2021). These predicted trends approximately correspond with the W to NW orientation of crisp ridges and scarps within Mare Tranquillitatis (Fig. 11), suggesting their formation is consistent with those models. However, it should be highlighted that the lithopsheric stressfield is a result from the complex interaction and overlaying of multiple stresses, evolving with time. Additional influences like, e.g., late stage mare basalt cooling (Tian et al. 2021), stresses related to a possible movement of magma in connection with young volcanic activity in Mare Tranquillitatis (Braden et al., 2014; Qiao et al., 2020), or preexisting ancient faults in the basement might have influenced the regional stress field. The patterns of moderately degraded wrinkle ridges allign with both the patterns of advanced and heavily degraded features, as well as with some crisp ridges and scarps (Fig. 4). Hence, moderately degraded wrinkle ridges and scarps could reflect the evolution of the stressfield from dominantly basin-localized to a dominately global stressfield, and they could represent the continued growth of ancient faults.

The large size and strongly degraded morphology of advanced and heavily degraded features suggest an older formation age relative to moderately degraded and crisp features. Advanced and heavily degraded features deform all the mare units defined by Hiesinger et al. (2000), which have ages of ~3.4 to ~3.8 Ga. Consequently, they have an upper formation age limit of at least 3.8 Ga. Since Rupes Cauchy and some large graben are deformed by advanced and heavily degraded wrinkle ridges, some of the wrinkle ridge formation occurred after 3.6 Ga (Lucchitta & Watkins, 1978; Watters et al., 2009). They can deform craters of several hundred meters in diameter but generally deform no craters, which agrees with Nectarian, Eratosthenian, and Imbrian formation ages (Trask, 1971). The deformation of craters with diameter ranges of hundreds of meters implies on the basis of crater degradation (Basilevsky, 1976, Fassett & Thomson, 2014) that at least some wrinkle ridges experienced ongoing activity throughout the Nectarian, Eratosthenian, and possibly even the Copernican. Yue et al. (2017) found a young average age of large wrinkle ridges in Mare Tranquillitatis (~2.4 Ga) relative to other lunar maria (~3.3 Ga). With the focus on Mare Tranquillitatis and the degradation-state approach of our classification, this age discrepancy between wrinkle ridges in Mare Tranquillitatis and other maria cannot be resolved. Relatively younger ages of advanced degraded wrinkle ridges compared to heavily degraded ridges can only be suggested and not conclusively proven. More precise dating methods than our morphological analysis are needed to uncover the early tectonic

evolution of the maria basins, however, standard CSFD measurements on wrinkle ridges are challenging, because of steep slopes, small count areas, and the often hummocky and heterogeneous terrain (Frueh et al., 2020). Hence, buffered crater counting might be a more suitable option to obtain formation ages of individual wrinkle ridges.

The occurrence of the advanced and heavily degraded concentric and radial wrinkle ridges in the western mare appears to have been localized by a subsurface feature (Fig. 9, 10; Freed et al., 2001; Schleicher et al., 2019). These concentric and radial wrinkle ridges, as well as several concentric large graben, can be attributed to the Lamont gravity anomaly, which is argued to be a ghost crater (Dvorak & Phillips, 1979; Scott, 1974) or a feature of volcanic origin (Zhang et al., 2018). Next to the Lamont anomaly, western Mare Tranquillitatis is characterized by a positive gravitational anomaly ranging from Mare Nectaris in the south to Mare Serenitatis in the north (Fig. 9, 10). Correlated with this positive anomaly are the thickest basalts in Mare Tranquillitatis (Dvorak & Phillips, 1979; De Hon, 1974, 2017; Konopliv et al., 2001; Zuber et al., 2013). At the surface, this positive anomaly is expressed as an elongated depression. Advanced and heavily degraded wrinkle ridges and large graben within this depression occur parallel to the gravitational anomaly and the topographic depression, which could also imply a subsidence-related origin (Fig. 3; McGovern et al., 2022). Mare Serenitatis most likely influenced the northwestern Mare Tranquillitatis, resulting in a radial wrinkle ridge and parallel graben to Mare Serenitatis (Fig. 3). Wrinkle ridges close to the eastern mare boundary follow a NS trend similar to the general trend of the eastern boundary itself, which is consistent with an origin from basin loading and subsidence. The eastern mare boundary shows no clearly detectable gravitational anomalies that have been associated with deep fractures of the mare basement (Fig. 10; Andrews-Hanna et al., 2018). The fewer number and the less coherent patterns of features in the eastern mare could be a result of the shallower basalts and, therefore, less basin loading induced by subsidence. While basin loading and subsidence influenced the regional stress field and the tectonic patterns in Tranquillitatis, additional global stress fields contributing to wrinkle ridge formation have been proposed. One possible influence on the global stress field are deep transient stresses generated by the South Pole-Aitken (SPA) basin (Schultz & Crawford, 2011), which predicts antipodal failures on the lunar nearside due to extensions deep within the Moon. Schultz and Crawford (2011) suggested reactivated deep-seated faults localized the wrinkle ridges. Wrinkle ridge patterns of the lunar nearside do spatially correlate with the predicted patterns (Schultz & Crawford, 2011; Valantinas & Schultz, 2020), however, it is not clear that SPA-related stresses would not have largely relaxed before the period of wrinkle ridge formation in Tranquillitatis. Another discussed potential model is the fault adjustment correlated with deep-seated intrusions on the lunar nearside. In this case, wrinkle ridges would be the surface expression of these deep-seated intrusions (Andrews-Hanna et al., 2014). GRAIL Bouguer gravity gradient data revealed a possible polygonal pattern of ancient deep intrusion connecting most of the lunar maria and also Mare Tranquillitatis (Andrews-Hanna et al., 2014). The western elongated positive gravitational anomaly of Mare Tranquillitatis is proposed to originate from these deep-seated intrusions. However, following the linear unrestricted growth trends and the similar displacement values of wrinkle ridges associated and not associated with these proposed intrusions, there is little evidence that most of the ridge faults were influenced by buried structures associated with ancient rifts (Watters, 2022). Having said that, we do observe wrinkle ridges correlated with sharp increases in elevation, possible extensive folding, and an elevation offset between both sites of the fold located in this western part of the basin. Possible similar wrinkle ridges have been associated

513 with deeply rooted faults penetrating the base of mare deposits (Byrne et al., 2015; Watters,
514 2022). The slopes of the trough associated with the positive gravitational anomaly, however,
515 complicates the assessment of the actual extent of folding. Quantifying the deformation in Mare
516 Tranquillitatis will be part of a planned follow-up study. In summary, the compressional stresses
517 that resulted in the formation of advanced and heavily degraded wrinkle ridges in Mare
518 Tranquillitatis originated primarily from load-induced subsidence with other possible sources of
519 regional or global stress, like SPA induced stress and fault adjustment, which changed with time.
520 Individual wrinkle ridges in western Tranquillitatis could be correlated to the deep-rooted faults.

521 It should be noted that the ancient age of advanced and heavily degraded feature, which
522 we we imply in this study, is the formation age and not necessarily the age of the most recent
523 activity along the fault. Previous studies discussed the possible activity of ancient wrinkle ridges
524 during the last Ma (French et al., 2019; Valantinas & Schultz, 2020). One possible evidence is
525 the abundance of boulders at wrinkle ridge crests (French et al., 2019; Valantinas et al., 2017;
526 Valantinas & Schultz, 2020; Watters et al., 2019). Valantinas and Schultz (2020) suggested that
527 layered mare basalts buckled and regolith drained into small fractures during episodes of uplift,
528 exposing the buckled material below. Basilevsky et al. (2013) and Ghent et al. (2014) found that
529 50% of rock populations, with fragment diameters larger than 2 m, are destroyed after 40 - 80
530 Ma and 99% after 150 - 300 Ma. Following the boulder size of wrinkle ridge boulder fields,
531 Valantinas and Schultz (2020) proposed that wrinkle ridges with high boulder abundance were
532 active during the last tens of millions of years. Boulder density increases with increasing slope.
533 This leads to the question whether boulders are simply associated with steep slopes rather than
534 ongoing wrinkle ridge activity since shallow seismic shaking generated by impacts or tectonic
535 activity unrelated to wrinkle ridges could also result in the exposure of boulder fields (French et
536 al., 2019). For our classification, the abundance of boulders was not used to determine the
537 possible erosional state of a wrinkle ridge segment. Crisp and moderately degraded features do
538 usually not appear in DiVINER rock abundance maps and boulders are only visible occasionally
539 in small patches. Thus, no or merely a few boulders have been exposed during their activity. This
540 could be either evidence against boulder fields as a general sign of recent tectonic activity,
541 related to the relation between flow thickness and thrust fault size, or correlated with the physical
542 properties of the basalt flows, which result in different predicted rock abundances (Elder et al.,
543 2022). Boulder-rich wrinkle ridges mapped by Valantinas and Schultz (2020) tend to correlate
544 with advanced degraded wrinkle ridges rather than heavily degraded. However, it should be
545 noted that the boulder fields themselves could influence the morphological classification since
546 they typically appear brighter than the regolith (Fig. 7a), possibly resulting in a greater contrast
547 between the sunlit and shadow side and, therefore, in a seemingly more defined appearance. Five
548 segments from Valantinas and Schultz (2020) can be associated with moderately degraded
549 wrinkle ridges. These are located at the southeastern Lamont ring and a single wrinkle ridge in
550 southwestern Mare Tranquillitatis (Fig. 12). All of these ridges occur together with advanced and
551 heavily degraded wrinkle ridges and are larger in relief than other moderately degraded features.
552 They deform craters with ~100 m in diameter or are accompanied by faint and small graben-like
553 features (Fig. 12b). The size of those moderately degraded wrinkle ridges, their transitional
554 morphology between moderately degraded and advanced degraded features, and their associated
555 patterns with advanced and heavily degraded wrinkle ridges suggest possible ancient wrinkle
556 ridges, which were later modified by more recent activity. Two large wrinkle ridges directly
557 north of the Lamont Anomaly could also contribute to this discussion (Fig. 3, 4, 9). The eastern
558 ridge (7.0°N, 22.7°E) shows a high boulder abundance, while the western ridge (7.0°N, 22.1°E)

559 only exhibits boulder fields in its northern most part (Valantinas & Schultz, 2020). Segments of
560 the eastern ridge are classified as advanced degraded and segments of the western ridge, mainly,
561 as heavily degraded. Additionally, the eastern wrinkle ridge shows one small off-shoot segments,
562 which is classified as moderately degraded (Fig. 4). The off-shoot segment could highlight a
563 continuing growth of the eastern wrinkle ridge, which resulted in the formation of boulder fields.
564 In those cases, boulder fields might be a sign of recent activity of the wrinkle ridges. However,
565 since boulders might also be exposed due to seismic shaking unrelated to wrinkle ridges (French
566 et al., 2019) and boulder fields can also be found on other positive relief features than wrinkle
567 ridges, we are not able to conclude if all boulder rich wrinkle ridges in Mare Tranquillitatis are
568 boulder-enriched due to their recent tectonic activity. In addition, crisp and moderately degraded
569 features have not exposed extensive boulder fields. Thus, we can neither clearly support nor
570 reject boulder fields along wrinkle ridges as a general sign of recent tectonism.

571 Boulder-rich wrinkle ridges on the lunar nearside are proposed to be part of an active
572 nearside tectonic system (ANTS). A possible origin for this recent activity was assigned to the
573 previously discussed deep transient stresses generated by the South Pole-Aitken (SPA) basin
574 (Schultz & Crawford, 2011; Valantinas & Schultz, 2020) and a continued fault adjustment
575 correlated with deep-seated intrusions (Andrews-Hanna et al., 2014; Valantinas & Schultz,
576 2020). Recorded deep moonquakes might be evidence of the SPA-induced stresses (Valantinas
577 & Schultz, 2020). However, as previously stated, the influence of these proposed putative mare-
578 filled ancient rifts and intrusions on wrinkle ridge formation has been questioned (Watters,
579 2022). Also, it remains unknown if the current lunar stress field would allow for ongoing
580 readjustment of those ancient faults. Thus, the question of young activity associated with ancient
581 wrinkle ridges and the implications of boulder fields remains unresolved. The reactivity or
582 prolonged activity of ancient wrinkle ridges, however, seems to be true for at least some
583 individual wrinkle ridges in Mare Tranquillitatis.

584

585 ## 5 Conclusions

586 In this study, compressional tectonic features were mapped in Mare Tranquillitatis and
587 classified into crisp, moderately degraded, advanced degraded, and heavily degraded, based on
588 their morphology and erosional state. This classification allows to suggest formation ages and
589 possible origins of these features:

590 - Crisp features show various signs of recent activity and presumably have an age of tens
591 of Ma (~50 Ma). Based on recent studies and the shared orientation of crisp features, they
592 likely formed due to a combination of global contraction and an additional influence of
593 tidal forces and/or SPA ejecta loading.

594 - Moderately degraded features, presumably, have a broad range of formation ages in
595 between crisp and advanced degraded features. They could reflect the evolution of the
596 stress field from dominantly basin-localized to a dominantly global stress field, and they
597 represent the continued growth of ancient faults.

598 - Advanced and heavily degraded features presumably formed in the early history of Mare
599 Tranquillitatis, starting at ~3.8 Ga. The distributions and orientations of these wrinkle
600 ridges indicate complex tectonic patterns and combined stresses. Ancient ridges in
601 western Mare Tranquillitatis have concentric, partly radial, and linear wrinkle ridge
602 patterns associated with basin loading and subsidence. There are scarce signs of recent
603 activity of some individual ancient wrinkle ridges within the last 100 Ma.

604 Mare Tranquillitatis exhibits compressional tectonic features with a variety of formation
605 ages ranging from ancient to recent. The complex and changing stress field behind wrinkle ridge
606 formation is presumably a result of a combination of different factors, which underlines the need
607 for new studies. Furthermore, our results highlight and strengthen the case for a still tectonically
608 active Moon within and outside of the maria basins. To further uncover the active lunar
609 tectonism, the future installation of a geophysical network on the Moon is highly desirable
610 (Fuqua Haviland et al., 2022).

Acknowledgments

The authors thank the LROC teams and LRO engineers for obtaining the essential data. We also thank the SELENE (KAGUYA) TC team and the SELENE Data Archive for providing the SELENE (KAGUYA) data. We acknowledge the use of imagery from Lunar QuickMap (https://quickmap.lroc.asu.edu), a collaboration between NASA, Arizona State University & Applied Coherent Technology Corp.

Data Availability Statement

Kaguya TC images can be obtained from the SELENE Data Archive (https://darts.isas.jaxa.jp/planet/pdap/selene/). The TC morning and evening image files can be downloaded from the *sln-1-tc-4-evening-map-v4.0/* and *sln-1-tc-4-morning-map-v4.0/* folders in the directory. LROC image data (Robinson, 2009) are available from the Lunar Orbital Data Explorer (https://ode.rsl.wustl.edu/moon/index.aspx), which is produced by the NASA Planetary Data System Geosciences Node (https://pds-geosciences.wustl.edu/). The SLDEM2015 global map (Neumann, 2009) is also available on the Planetary Data System (pds-geosciences.wustl.edu - /lro/lro-l-lola-3-rdr-v1/lrolol_1xxx/data/sldem2015/), as well as the derived GRAIL data (Kahan, 2013; pds-geosciences.wustl.edu-/grail/grail-l-lgrs-5-rdr-v1/grail_1001/). Global GRAIL maps can be downloaded in the rsdmap directory. The GRAIL bouguer gravity gradient map was accessed from the supplementary material from Andrews-Hanna et al. (2018; https://data.mendeley.com/datasets/pz874f2bs2/1). Additionally, LRO, Kaguya, and GRAIL data can be accessed with Quickmap (https://quickmap.lroc.asu.edu). The shown rose diagram was created with GeoRose 0.5.1 (http://www.yongtechnology.com/georose/).

References

Andrews-Hanna, J. C., Asmar, S. W., Head, J. W., Kiefer, W. S., Konopliv, A. S., Lemoine, F. G., Matsuyama, I., Mazarico, E., McGovern, P. J., Melosh, H. J., Neumann, G. A., Nimmo, F., Phillips, R. J., Smith, D. E., Solomon, S. C., Taylor, G. J., Wieczorek, M. A., Williams, J. G., & Zuber, M. T. (2013). Ancient Igneous Intrusions and Early Expansion of the Moon Revealed by GRAIL Gravity Gradiometry. *Science*, *339(6120)*, 675–678. https://doi.org/10.1126/science.1231753

Andrews-Hanna, J. C., Besserer, J., Head, J. W., Howett, C. J. A., Kiefer, W. S., Lucey, P. J., et al. (2014). Structure and evolution of the lunar Procellarum region as revealed by GRAIL gravity data. *Nature*, *514*(7520), 68–71. https://doi.org/10.1038/nature13697

Andrews-Hanna, J. C., Head, J. W., Johnson, B. C., Keane, J. T., Kiefer, W. S., McGovern, P. J., Neumann, G. A., Wieczorek, M. A., & Zuber, M. T. (2018). Ring faults and ring dikes around the Orientale basin on the Moon. *Icarus, 310*, 1–20. https://doi.org/https://doi.org/10.1016/j.icarus.2017.12.012

Arvidson, R., Drozd, R. J., Hohenberg, C. M., Morgan, C. J., & Poupeau, G. (1975). Horizontal transport of the regolith, modification of features, and erosion rates on the lunar surface. *The Moon*, *13*, 67–79. https://doi.org/10.1007/BF00567508

Barker, M. K., Mazarico, E., Neumann, G. A., Zuber, M. T., Haruyama, J., & Smith, D. E. (2016). A new lunar digital elevation model from the Lunar Orbiter Laser Altimeter and SELENE Terrain Camera. *Icarus*, *273*, 346–355. https://doi.org/10.1016/j.icarus.2015.07.039

Basilevsky, A. T. (1976). On the evolution rate of small lunar craters. *Proceeding Lunar Science Conference, 7*, 1005–1020.

656 Basilevsky, A. T., Head, J. W., & Horz, F. (2013). Survival times of meter-sized boulders on the
657 surface of the Moon. *Planetary and Space Science*, *89*, 118–126.
658 https://doi.org/10.1016/j.pss.2013.07.011
659 Bhatt, H., Chauhan, P., & Solanki, P. (2020). Compositional mapping and the evolutionary
660 history of Mare Tranquillitatis. *Journal of Earth System Science*, *129*, 45.
661 https://doi.org/10.1007/s12040-019-1302-7
662 Bickel, V. T., Aaron, J., Manconi, A., & Loew, S. (2021). Global Drivers and Transport
663 Mechanisms of Lunar Rockfalls. *Journal of Geophysical Research: Planets, 126(10)*.
664 https://doi.org/10.1029/2021JE006824
665 Binder, A. B., & Gunga, H. C. (1985). Young thrust-fault scarps in the highlands: evidence for
666 an initially totally molten moon. *Icarus*, *63*(3), 421–441. https://doi.org/10.1016/0019-
667 1035(85)90055-7
668 Bondarenko, N. v, Kreslavsky, M. A., Zubarev, A., & Nadezhdina, I. (2022). "ELEPHANT
669 HIDE" TEXTURE ON THE MOON: PRELIMINARY RESULTS ON TOPOGRAPHIC
670 PROPERTIES. In *53rd Lunar and Planetary Science Conference*, Abstract #2469
671 van der Bogert, C. H., Clark, J. D., Hiesinger, H., Banks, M. E., Watters, T. R., & Robinson, M.
672 S. (2018). How old are lunar lobate scarps? 1. Seismic resetting of crater size-frequency
673 distributions. *Icarus*, *306*, 225–242. https://doi.org/10.1016/j.icarus.2018.01.019
674 Braden, S. E., Stopar, J. D., Robinson, M. S., Lawrence, S. J., Van Der Bogert, C. H., &
675 Hiesinger, H. (2014). Evidence for basaltic volcanism on the Moon within the past 100
676 million years. *Nature Geoscience*, *7*(11), 787–791. https://doi.org/10.1038/ngeo2252
677 Byrne, P. K., Klimczak, C., McGovern, P. J., Mazarico, E., James, P. B., Neumann, G. A., et al.
678 (2015). Deep-seated thrust faults bound the Mare Crisium lunar mascon. *Earth and*

Planetary Science Letters, *427*, 183–190. https://doi.org/10.1016/j.epsl.2015.06.022

Clark, J. D., Hurtado, J. M., Hiesinger, H., van der Bogert, C. H., & Bernhardt, H. (2017). Investigation of newly discovered lobate scarps: Implications for the tectonic and thermal evolution of the Moon. *Icarus*, *298*, 78–88. https://doi.org/10.1016/j.icarus.2017.08.017

Clark, J. D., Van Der Bogert, C. H., Hiesinger, H., Watters, T. R., & Robinson, M. S. (2019). Fault Slip Movement Along Wrinkle Ridge-Lobate Scarp Transitions in the Last 100 Ma. In *50th Lunar and Planetary Science Conference*, Abstract #2084.

Daket, Y., Yamaji, A., Sato, K., Haruyama, J., Morota, T., Ohtake, M., & Matsunaga, T. (2016). Tectonic evolution of northwestern Imbrium of the Moon that lasted in the Copernican Period. *Earth, Planets and Space*, *68*, 157. https://doi.org/10.1186/s40623-016-0531-0

Dvorak, J., & Phillips, R. J. (1979). Gravity anomaly and structure associated with the Lamont region of the moon. In *10th Lunar and Planetary Science Conference*, 2265–2275.

Elder, C. M., Haber, J., Hayne, P. O., Ghent, R. R., Williams, J.-P., & Siegler, M. A. (2022). INFERRING LUNAR MARE BASALT MATERIAL PROPERTIES FROM SURFACE ROCK ABUNDANCE. In *53rd Lunar and Planetary Science Conference*, Abstract #2360.

Fagin, S. W., Worrall, D. M., & Muehlberger, W. R. (1978). Lunar mare ridge orientations: implications for lunar tectonic models. In *9th Lunar and Planetary Science Conference*, 3473–3479.

Fassett, C. I., & Thomson, B. J. (2014). Crater degradation on the lunar maria: Topographic diffusion and the rate of erosion on the Moon. *Journal of Geophysical Research: Planets, 119(10)*, 2255–2271. https://doi.org/10.1002/2014JE004698

Freed, A. M., Melosh, H. J., & Solomon, S. C. (2001). Tectonics of mascon loading: Resolution of the strike-slip faulting paradox. *Journal of Geophysical Research*, *106*(E9), 20603–

20620. https://doi.org/10.1029/2000JE001347

French, R. A., Bina, C. R., Robinson, M. S., & Watters, T. R. (2015). Small-scale lunar graben: Distribution, dimensions, and formation processes. *Icarus*, *252*, 95–106. https://doi.org/10.1016/j.icarus.2014.12.031

French, R. A., Watters, T. R., & Robinson, M. S. (2019). Provenance of Block Fields Along Lunar Wrinkle Ridges. *Journal of Geophysical Research: Planets*, *124*, 2970–2982. https://doi.org/10.1029/2019JE006018

Frueh, T., van der Bogert, C. H., Hiesinger, H., & Schmedemann, N. (2020). Reassessment of Indivudal Lunar Wrinkle Ridge Ages in Mare Tranquillitatis. In *51st Lunar and Planetary Science Conference*, Abstract #1854.

Fuqua Haviland, H., Weber, R. C., Neal, C. R., Lognonné, P., Garcia, R. F., Schmerr, N., et al. (2022). The Lunar Geophysical Network Landing Sites Science Rationale. *The Planetary Science Journal*, 3(2), 40. https://doi.org/10.3847/psj/ac0f82

Ghent, R. R., Hayne, P. O., Bandfield, J. L., Campbell, B. A., Allen, C. C., Carter, L. M., & Paige, D. A. (2014). Constraints on the recent rate of lunar ejecta breakdown and implications for crater ages. *Geology*, *42(12),* 1059–1062. https://doi.org/10.1130/G35926.1

Gold, T. (1972). Erosion, Transportation and the Nature of the Maria. In Runcorn, S. K., Urey, H. C. (Eds), *The Moon. International Astronomical Union/Union, 47,* 55–67. https://doi.org/doi:10.1017/S0074180900097424

Golombek, M. P., Plescia, J. B., & Franklin, B. J. (1991). Faulting and Folding in the Formation of Planetary Wrinkle Ridges. *Proceedings of Lunar and Planetary Science*, *21*, 679–693.

Hiesinger, H., Jaumann, R., Neukum, G., & Head, J. W. (2000). Ages of mare basalts on the lunar nearside. *Journal of Geophysical Research*, *105*(E12), 29239–29275.

https://doi.org/10.1029/2000JE001244

Hiesinger, H., Head, J. W., Wolf, U., Jaumann, R., & Neukum, G. (2011). Ages and stratigraphy of lunar mare basalts: A synthesis. *Recent Advances and Current Research Issues in Lunar Stratigraphy: Geological Society of America Special Paper 477, 477*, 1–51. https://doi.org/10.1130/2011.2477(01)

De Hon, R. A. (1974). Thickness of mare material in the Tranquillitatis and Nectaris basins. In *5th Lunar and Planetary Science Conference*, 53–59.

De Hon, R. A. (2017). A Two-Basin Model For Mare Tranquillitatis. In *48th Lunar and Planetary Science Conference*, Abstract #2769.

Ikeda, A., Kumagai, H., & Morota, T. (2022). Topographic Degradation Processes of Lunar Crater Walls Inferred From Boulder Falls. *Journal of Geophysical Research: Planets, 127(10)*. https://doi.org/10.1029/2021je007176

Iqbal, W., Hiesinger, H., & van der Bogert, C. H. (2019). Geological mapping and chronology of lunar landing sites: Apollo 11. *Icarus*, *333*, 528–547. https://doi.org/https://doi.org/10.1016/j.icarus.2019.06.020

Kahan, D. S. (2013). GRAIL Moon LGRS Derived Gravity Science Data Products V1.0, GRAIL-L-LGRS-5-RDR-V1.0 [Dataset]. *NASA Planetary Data System*. https://doi.org/ 10.17189/1519529

Konopliv, A. S., Asmar, S. W., Carranza, E., Sjogren, W. L., & Yuan, D. N. (2001). Recent gravity models as a result of the Lunar Prospector mission. *Icarus*, *150*(1), 1–18. https://doi.org/10.1006/icar.2000.6573

Lu, Y., Wu, Y., Michael, G. G., Basilevsky, A. T., & Li, C. (2019). Young wrinkle ridges in Mare Imbrium: Evidence for very recent compressional tectonism. *Icarus*, *329*, 24–33.

https://doi.org/10.1016/j.icarus.2019.03.029

Lucchitta, B. K. (1976). Mare ridges and related highland scarps-Result of vertical tectonism? In *7th Lunar and Planetary Science Conference*, 2761–2782.

Lucchitta, B. K., & Watkins, J. A. (1978). Age of graben systems on the moon. In *9th Lunar and Planetary Science Conference*, 3459–3472.

Matsuyama, I., Keane, J. T., Trinh, A., Beuthe, M., & Watters, T. R. (2021). Global tectonic patterns of the Moon. *Icarus*, *358*, 114202. https://doi.org/10.1016/j.icarus.2020.114202

McGovern, P. J., Kramer, G. Y., & Neumann, G. A. (2022). Delayed onset of wrinkle ridge formation in mare tranquillitatis: a manifestation of lunar thermo-chemical evolution. In 53 rd *Lunar and Planetary Science Conference*, Abstract #2853.

Montési, L. G. J., & Zuber, M. T. (2003). Clues to the lithospheric structure of Mars from wrinkle ridge sets and localization instability. *Journal of Geophysical Research*, *108*(E6), 5048. https://doi.org/10.1029/2002je001974

Muller, P. M., & Sjogren, W. L. (1968). Mascons: Lunar Mass Concentrations. *Science, 161(3842)*, 680–684. https://doi.org/https://doi.org/10.1126/science.161.3842.680

Nelson, D. M., Koeber, S. D., Daud, K., Robinson, M. S., Watters, T. R., Banks, M. E., & Williams, N. R. (2014). Mapping lunar maria extents and lobate scarps using LROC image products. In *45th Lunar and Planetary Science Conference,* Abstract #2861.

Neumann, G.A. (2009). Lunar Orbiter Laser Altimeter Raw Data Set, LRO-L-LOLA-4-GDR-V1.0 [Dataset]. *NASA Planetary Data System*. https://doi.org/10.17189/1520642

Nypaver, C. A., & Thomson, B. J. (2022). New observations of recently active wrinkle ridges in the lunar mare: Implications for the timing and origin of lunar tectonics. *Geophysical Research Letters, 49*. https://doi.org/10.1029/2022GL098975

771 Ohtake, M., Haruyama, J., Matsunaga, T., Yokota, Y., Morota, T., & Honda, C. (2008).
772 Performance and scientific objectives of the SELENE (KAGUYA) multiband imager.
773 *Earth, Planets and Space*, *60*(4), 257–264. https://doi.org/10.1186/BF03352789
774 Okubo, C. H., & Schultz, R. A. (2003). Two-Dimensional Wrinkle Ridge Strain & Energy
775 Release Based on Numerical Modeling of MOLA Topography. In *34th Lunar and*
776 *Planetary Science Conference*, Abstract #1283.
777 Okubo, C. H., & Schultz, R. A. (2004). Mechanical stratigraphy in the western equatorial region
778 of Mars based on thrust fault-related fold topography and implications for near-surface
779 volatile reservoirs. *Bulletin of the Geological Society of America*, *116*(5/6), 594–605.
780 https://doi.org/10.1130/B25361.1
781 Ono, T., Kumamoto, A., Nakagawa, H., Yamaguchi, Y., Oshigami, S., Yamaji, A., et al. (2009).
782 Lunar radar sounder observations of subsurface layers under the nearside maria of the
783 moon. *Science*, *323*(5916), 909–912. https://doi.org/10.1126/science.1165988
784 Plescia, J. B., & Golombek, M. P. (1986). Origin of Planetary Wrinkle Ridges Based on the
785 Study of Terrestrial Analogs. *Bulletin of the Geological Society of America*, *97*(11), 1289–
786 1299. https://doi.org/10.1130/0016-7606(1986)97<1289:oopwrb>2.0.co;2
787 Qiao, L., Head, J. W., Wilson, L., & Ling, Z. (2020). The Cauchy 5 Small, Low-Volume Lunar
788 Shield Volcano: Evidence for Volatile Exsolution-Eruption Patterns and Type 1/Type 2
789 Hybrid Irregular Mare Patch Formation. *Journal of Geophysical Research: Planets*, *125*, 1–
790 28. https://doi.org/10.1029/2019JE006171
791 Rajmon, D., & Spudis, P. (2004). Distribution and stratigraphy of basaltic units in Maria
792 Tranquillitatis and Fecunditatis: A Clementine perspective. *Meteoritics and Planetary*
793 *Science*, *39*(10), 1699–1720. https://doi.org/10.1111/j.1945-5100.2004.tb00067.x

Robinson, M. (2009). LRO MOON LROC 5 RDR V1.0 [Dataset]. *NASA Planetary Data System (PDS)*. https://doi.org/10.17189/1520341

Robinson, M. S., Speyerer, E. J., Boyd, A., Waller, D., Wagner, R. V., & Burns, K. N. (2012). Exploring the Moon With the Lunar Reconnaissance Orbiter Camera. *ISPRS - International Archives of the Photogrammetry, Remote Sensing and Spatial Information Sciences*, *XXXIX*, 501–504. https://doi.org/10.5194/isprsarchives-xxxix-b4-501-2012

Schleicher, L. S., Watters, T. R., Martin, A. J., & Banks, M. E. (2019). Wrinkle ridges on Mercury and the Moon within and outside of mascons. *Icarus*, *331*, 226–237. https://doi.org/10.1016/j.icarus.2019.04.013

Schultz, P. H., & Crawford, D. A. (2011). Origin of nearside structural and geochemical anomalies on the Moon. *Recent Advances and Current Research Issues in Lunar Stratigraphy: Geological Society of America Special Paper*, *477*, 141–159. https://doi.org/10.1130/2011.2477(07)

Schultz, R. A. (2000). Localization of bedding plane slip and backthrust faults above blind thrust faults: Keys to wrinkle ridge structure. *Journal of Geophysical Research E: Planets*, *105*(E5), 12035–12052. https://doi.org/10.1029/1999JE001212

Scott, D. H. (1974). The geologic significance of some lunar gravity anomalies. In *5th Lunar and Planetary Science Conference*, 3025–3036.

Sharpton, V. L., & Head, J. W. (1988). Lunar Mare Ridges: Analysis of Ridge-Crater Intersections and Implications for the Tectonic Origin of Mare Ridges. In *18th Lunar and Planetary Science Conference*, 307–317.

Solomon, S. C. (1986). On the early thermal state of the moon. In *Origin of the moon*, 435–452. Houston, Texas: Lunar and Planetary Institute.

817 Solomon, Sean C., & Head, J. W. (1979). Vertical movement in mare basins: Relation to mare
818 emplacement, basin tectonics, and lunar thermal history. *Journal of Geophysical Research*,
819 *84*(B4), 1667–1682. https://doi.org/10.1029/jb084ib04p01667
820 Spudis, P. D. (1993). From crater to basin. In *The Geology of Multi-Ring Impact Basins*, 18–41.
821 Cambridge: Cambridge University Press. https://doi.org/10.1017/cbo9780511564581.003
822 Spudis, P. D., McGovern, P. J., & Kiefer, W. S. (2013). Large shield volcanoes on the Moon.
823 *Journal of Geophysical Research: Planets*, *118*, 1063–1081.
824 https://doi.org/10.1002/jgre.20059
825 Stöffler, D., Ryder, G., Ivanov, B. A., Artemieva, N. A., Cintala, M. J., & Grieve, R. A. F.
826 (2006). Cratering history and Lunar Chronology. *Reviews in Mineralogy and Geochemistry*,
827 *60*. https://doi.org/10.2138/rmg.2006.60.05
828 Strom, R. G. (1972). Lunar mare ridges, rings and volcanic ring complexes. In Runcorn, S. K.,
829 Urey, H. C. (Eds), *The Moon. International Astronomical Union*, *47*, 187–215.
830 https://doi.org/10.1007/978-94-010-2861-5_19
831 Tian, H. C., Wang, H., Chen, Y., Yang, W., Zhou, Q., Zhang, C., Lin, H. L., Huang, C., Wu, S.
832 T., Jia, L. H., Xu, L., Zhang, D., Li, X. G., Chang, R., Yang, Y. H., Xie, L. W., Zhang, D.
833 P., Zhang, G. L., Yang, S. H., & Wu, F. Y. (2021). Non-KREEP origin for Chang'e-5
834 basalts in the Procellarum KREEP Terrane. *Nature*, *600*(7887), 59–63.
835 https://doi.org/10.1038/s41586-021-04119-5
836 Trask, N. J. (1971). Geologic comparison of mare materials in the lunar equatorial belt, including
837 Apollo 11 and Apollo 12 landing sites. *Geological Survey Research*, *750*, 138-144.
838 Valantinas, A., & Schultz, P. H. (2020). The origin of neotectonics on the lunar nearside.
839 *Geology*, *48*, 649–653. https://doi.org/10.1130/g47202.1

Valantinas, A., Kinch, K. M., & Bridžius, A. (2017). Rocky outcrops and low crater densities on lunar wrinkle ridges: Evidence for recent tectonic activity? *European Planetary Science Congress 2017*, *11*, Abstract #961.

Valantinas, A., Kinch, K.M. and Bridžius, A. (2018), Low crater frequencies and low model ages in lunar maria: Recent endogenic activity or degradation effects?. *Meteorit Planet Sci, 53*, 826-838. https://doi.org/10.1111/maps.13033

Watters, T. R. (1988). Wrinkle ridge assemblages on the terrestrial planets. *Journal of Geophysical Research*, *93*(B9), 10236–10254. https://doi.org/10.1029/jb093ib09p10236

Watters, T. R. (2004). Elastic dislocation modeling of wrinkle ridges on Mars. *Icarus*, *171*(2), 284–294. https://doi.org/10.1016/j.icarus.2004.05.024

Watters, T. R. (2022). Lunar Wrinkle Ridges and the Evolution of the Nearside Lithosphere. *Journal of Geophysical Research: Planets*, *127*(3). https://doi.org/10.1029/2021je007058

Watters, T. R., & Johnson, C. (2009). Lunar tectonics. In Watters, T. R., and Schultz, R. (Eds.), *Planetary Tectonics*. Cambridge, Cambridge University Press.

Watters, T. R., Robinson, M. S., Beyer, R. A., Banks, M. E., Bell, J. F., Pritchard, M. E., et al. (2010). Evidence of recent thrust faulting on the moon revealed by the lunar reconnaissance orbiter camera. *Science*, *329*(5994), 936–940. https://doi.org/10.1126/science.1189590

Watters, T. R., Robinson, M. S., Banks, M. E., Tran, T., & Denevi, B. W. (2012). Recent extensional tectonics on the Moon revealed by the Lunar Reconnaissance Orbiter Camera. *Nature Geoscience*, *5*(3), 181–185. https://doi.org/10.1038/ngeo1387

Watters, T. R., Robinson, M. S., Collins, G. C., Banks, M. E., Daud, K., Williams, N. R., & Selvans, M. M. (2015). Global thrust faulting on the Moon and the influence of tidal stresses. *Geology*, *43*(10), 851–854. https://doi.org/10.1130/G37120.1

Watters, T. R., Weber, R. C., Collins, G. C., Howley, I. J., Schmerr, N. C., & Johnson, C. L. (2019). Shallow seismic activity and young thrust faults on the Moon. *Nature Geoscience*, *12*(6), 411–417. https://doi.org/10.1038/s41561-019-0362-2

Whitaker, E. A. (1981). The lunar Procellarum basin. In Schultz, P. H., and Merrill, R. B. (Eds.), Multi-Ring Basins: Formation and Evolution, *Proc. Lunar Planet. Sci*. New York and Oxford, Pergamon Press, 105–111.

Wieczorek, M. A., & Phillips, R. J. (2000). The "Procellarum KREEP Terrane": Implications for mare volcanism and lunar evolution. *Journal of Geophysical Research*, *105*(E8), 20417–20430.

Wilhelms, D., McCauley, J., & Trask, N. (1987). *The geological history of the moon*. Washington, DC: US Government Printing Office.

Williams, N. R., Watters, T. R., Pritchard, M. E., Banks, M. E., & Bell, J. F. (2013). Fault dislocation modeled structure of lobate scarps from Lunar Reconnaissance Orbiter Camera digital terrain models. *Journal of Geophysical Research: Planets*, *118*(2), 224–233. https://doi.org/10.1002/jgre.20051

Williams, N. R., Bell, J. F., Watters, T. R., Banks, M. E., Daud, K., & French, R. A. (2019). Evidence for recent and ancient faulting at Mare Frigoris and implications for lunar tectonic evolution. *Icarus*, *326*, 151–161. https://doi.org/10.1016/j.icarus.2019.03.002

Yue, Z., Michael, G. G., Di, K., & Liu, J. (2017). Global survey of lunar wrinkle ridge formation times. *Earth and Planetary Science Letters*, *477*, 14–20. https://doi.org/10.1016/j.epsl.2017.07.048

Zhang, F., Zhu, M. H., Bugiolacchi, R., Huang, Q., Osinski, G. R., Xiao, L., & Zou, Y. L. (2018). Diversity of basaltic lunar volcanism associated with buried impact structures:

Implications for intrusive and extrusive events. *Icarus*, *307*, 216–234. https://doi.org/10.1016/j.icarus.2017.10.039

Zuber, M. T., Smith, D. E., Watkins, M. M., Asmar, S. W., Konopliv, A. S., Lemoine, F. G., et al. (2013). Gravity field of the moon from the Gravity Recovery and Interior Laboratory (GRAIL) mission. *Science*, *339*(6120), 668–671. https://doi.org/10.1126/science.1231507

Zharkova, A. Yu., Kreslavsky, M. A., Head, J. W., & Kokhanov, A. A. (2020). Regolith textures on Mercury: Comparison with the Moon. *Icarus, 351*, 113945. https://doi.org/https://doi.org/10.1016/j.icarus.2020.113945

Figure 1. Schematic model of the signs of recent tectonic activity of surface features. A small crisp wrinkle ridge segment in Mare Tranquillitatis served as a template for the topographic profile. The signs of recent tectonic activity apply, however, both for lobate scarps and wrinkle ridges. These signs include crisp morphology, deformed craters, cross-cut craters, small graben and troughs, lower crater density, and boulder fields/patches. In this study, the boulder abundance was not used to determine the degradational stage of a wrinkle ridge or lobate scarp. Shallow moonquakes detected by the Apollo missions have been previously correlated to the activity of lobate scarps.

Figure 2. a) Location of Mare Tranquillitatis (white outline; Nelson et al., 2014) near the lunar equator projected onto the global merged WAC mosaic. b) Mare Tranquillitatis (black outline) projected onto the LRO LOLA – SELENE Kaguya DEM (Neumann, 2009; Barker et al., 2016). A color-blindness-friendly version can be accessed in the supplementary materials (Fig. S1). c) The black outline of Mare Tranquillitatis projected onto the GRAIL Free Air Gravity map (Kahan, 2013; harmonic degree and order of 660). The black lines sketch the proposed quasi-rectangular pattern of ancient intrusion (after Andrews-Hanna et al., 2012).

Figure 3. Tectonic map of Mare Tranquillitatis projected on the merged LRO LOLA – SELENE Kaguya DEM (Barker et al., 2016). A color-blindness-friendly version can be accessed in the supplementary materials (Fig. S2). Parts of the lobate scarp cluster in the northern mare cross the highland boundary and continue into Mare Serenitatis near the Taurus-Littrow valley. Unidentified features are linear positive topographic features with a possible but unproven tectonic origin (other possible origins are, e.g., dikes, lava flows, surface expressions of buried structures, or ejecta remnants).

Figure 4. Tectonic feature map with all degradational classified segments colorized according to their respective class and projected onto the WAC global mosaic (Robinson et al., 2012). This map includes wrinkle ridge, lobate scarp, and unidentified features. Tectonic features in the western part are mostly comprised of advanced and heavily degraded features. Crisp and moderately degraded features occur scattered in clusters throughout the mare.

Figure 5. NAC images of crisp features. White arrows show representative graben. a) Wrinkle ridge north of Ross Crater with a crisp morphology and small graben (M1184668142RE; 11.82°N, 24.27°E). b) Image of the same wrinkle ridge further west. Visible are several sets of small graben and a small boulder patch (black arrow; M1184668142RE; 11.90°N, 24.17°E). c) Small and faint lobate scarp in the vicinity of Taurus-Littrow valley. The image shows some faint graben-like features and deformed craters with ~100 to ~50 m in diameter (black arrows; M1154023134RE; 19.11°N, 29.93°E). d) Set of graben in close vicinity of a crisp lobate scarp cluster near Taurus-Littrow (M1157549836RE; 18.52°N, 30.55°E).

935

936 **Figure 6**. NAC images of moderately degraded features with relatively sharp contacts (white
937 arrows) in Mare Tranquillitatis. a) A moderately degraded wrinkle ridge in the eastern mare
938 deforming and cross-cutting several craters (black arrows; M1245756057LE/RE; 12.29°N,
939 39.82°E) and b) a small moderately degraded lobate scarp in the northwestern mare which also
940 deforms a ~100 m diameter crater (black arrows; M1279976340LE; 14.60°N, 20.04°E).
941

942 **Figure 7**. Kaguya Terrain Camera images of a representative advanced degraded wrinkle ridges.
943 The advanced degraded wrinkle ridge (7.54°N, 22.75°E) has a well-developed wrinkle ridge
944 morphology consisting of a broad arch and a superimposed ridge (white arrows). In addition, it
945 exhibits several dominant boulder fields, which are visible as bright spots along the ridge (black
946 arrows). b) Close up NAC image (M1234102538LE) of the ridge shown in 7a, featuring boulder
947 fields (black arrow) and the "elephant-hide" texture (white arrows).

948

949

950 **Figure 8**. Kaguya Terrain Camera images of representative heavily degraded wrinkle ridges
951 (white arrows). Both wrinkle ridges (a), 1.31°N, 22.56°E; b), 8.10°N, 22.20°E) have gentle
952 slopes and less well-developed wrinkle ridge morphologies than seen in figure 7. The ~1 km
953 sized crater in the center of image a) resembles a rare case, which shows the possible
954 deformation of a crater by a heavily degraded ridge. Survival times of ~1 km sized craters are
955 still estimated to be several billion years (Fassett & Thomson, 2014).

956

957 **Figure 9**. Bouguer anomaly map of Tranquillitatis superposed on the WAC global mosaic. The
958 map has the same spatial extent as the map in Fig. 4, and shows the tectonic feature map of Fig.
959 4. The outline of Mare Tranquillitatis is shown as a fine white line. Yellowish colors indicate
960 positive gravitational anomalies, which implies a thin crust and mantle upwelling, as well as a
961 thick abundance of basalt. Mascon basins like Mare Serenitatis in the northwestern part of the
962 map are represented in yellow colors, whereas non-mascon basins like Mare Tranquillitatis
963 appear in more heterogenous and mainly blue and green colors. The western part of Mare
964 Tranquillitatis has more pronounced positive gravitational anomalies than the eastern part.
965 Concentric wrinkle ridges occur at the positive Lamont anomaly in southwestern Tranquillitatis.
966 Crisp and moderately degraded features are not correlated with gravitational anomalies.

967

968 **Figure 10.** Grail bouguer gravity gradients map of Mare Tranquillitatis (supplement material
969 from Andrews-Hanna et al., 2018) in units of Eötvös (1 E = 10^{-9} s^{-2}) and our tectonic map of
970 Fig. 3. Gravity gradient maps are used to identify buried deep-seated structures, like large
971 igneous intrusions and ring-faults in impact basins (e.g., Andrews-Hanna et al., 2013, 2014,
972 2018; Valantinas & Schultz, 2020). Eastern Tranquillitatis does not exhibit clearly detectable
973 anomalies known from deep faults.

974

975 **Figure 11**. Rose diagram of the orientations of crisp features within Mare Tranquillitatis,
976 including lobate scarps and wrinkle ridges. Crips features share a western to northwestern
977 orientation.

978

979 **Figure 12**. Evidence for recent activity by ancient wrinkle ridges in Mare Tranquillitatis. (a)
980 Shows the topographic map of the region southeast of the Lamont anomaly. The stars mark the
981 locations of (b) and (c). (b) Shows NAC image (M1108125194LE; 3.43°N, 23.97°E) showing a
982 part of a concentric wrinkle ridge at the southeastern Lamont anomaly. It crosscuts craters with
983 ~100 m in diameter (white arrow) and exhibits several boulder fields (black arrows). (c) NAC
984 image (M162134363LE) of faint graben-like features on the hanging wall of a wrinkle ridge
985 (0.45°S, 26.47°E). A color-blindness-friendly version can be accessed in the supplementary
986 materials (Fig. S3).

Figure 1.

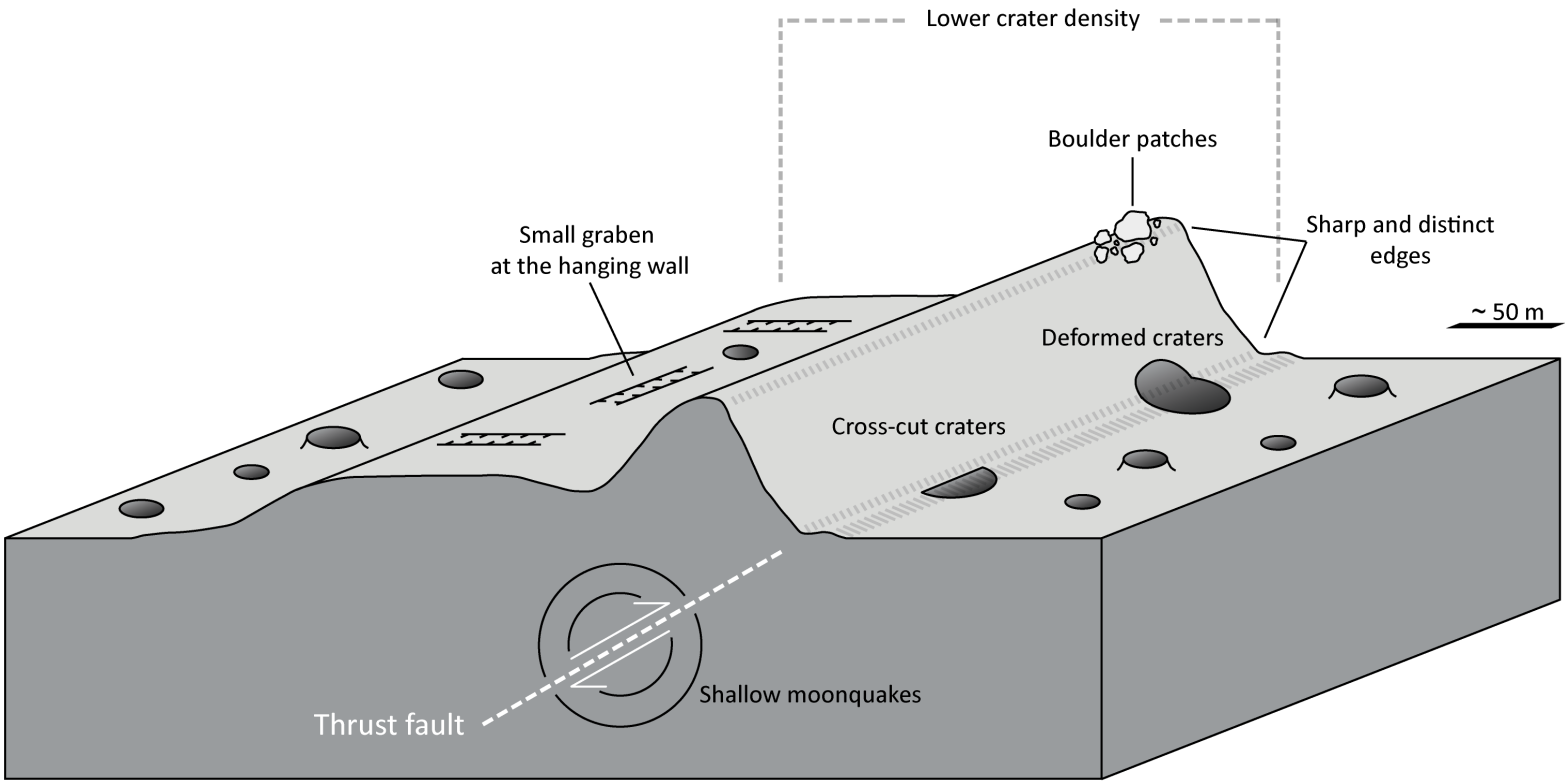
Lower crater density
Boulder patches
Small graben
at the hanging wall
Sharp and distinct
edges
~ 50 m
Deformed craters
Cross-cut craters
Shallow moonquakes
Thrust fault

Figure 2.

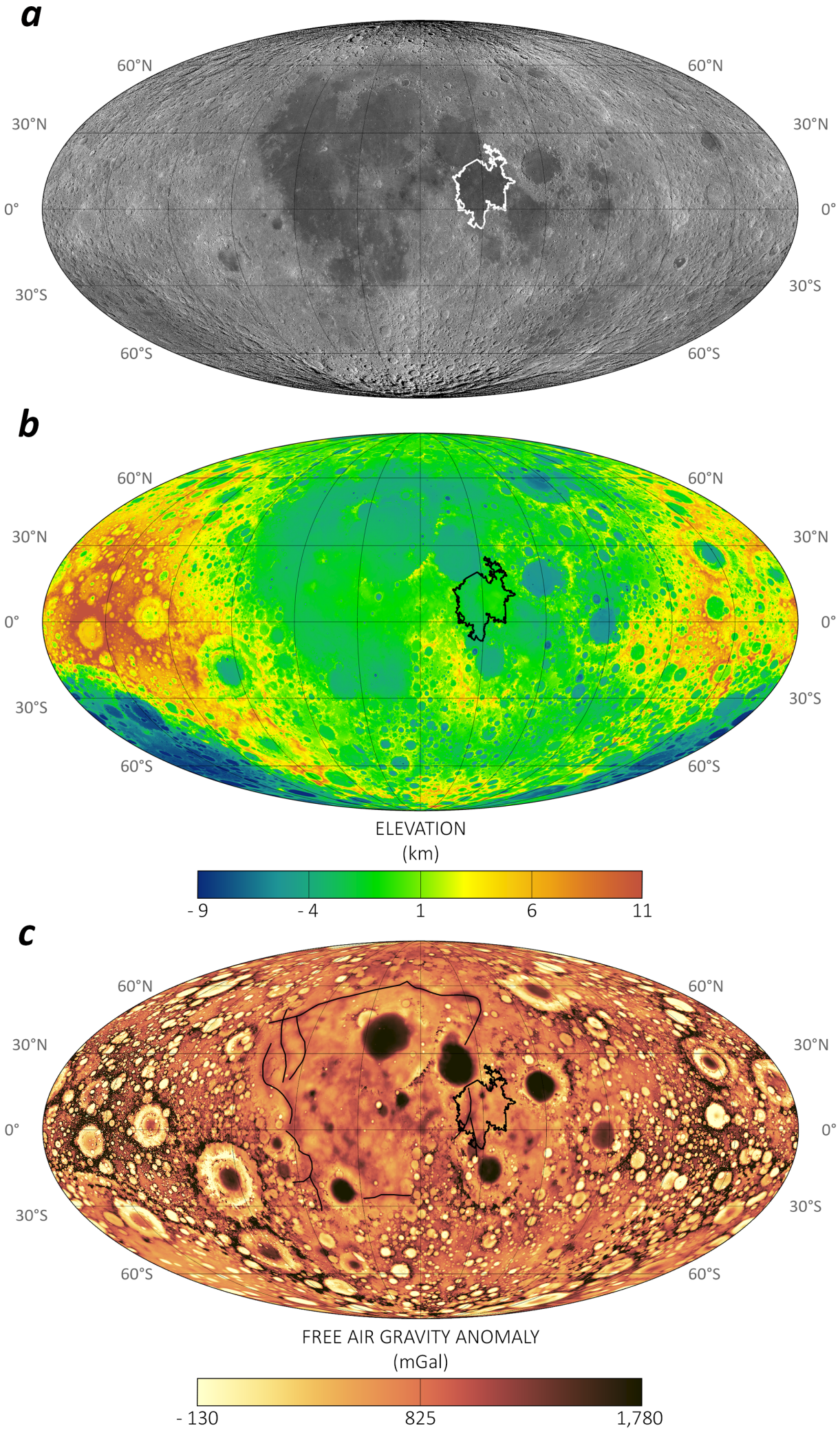
a
60°N
60°N
30°N
30°N
0°
0°
30°S
30°S
60°S
60°S
b
60°N
60°N
30°N
30°N
0°
0°
30°S
30°S
60°S
60°S
ELEVATION
(km)
- 9
- 4
1
6
11
c
60°N
60°N
30°N
30°N
0°
0°
30°S
30°S
60°S
60°S
FREE AIR GRAVITY ANOMALY
(mGal)
- 130
825
1,780

Figure 3.

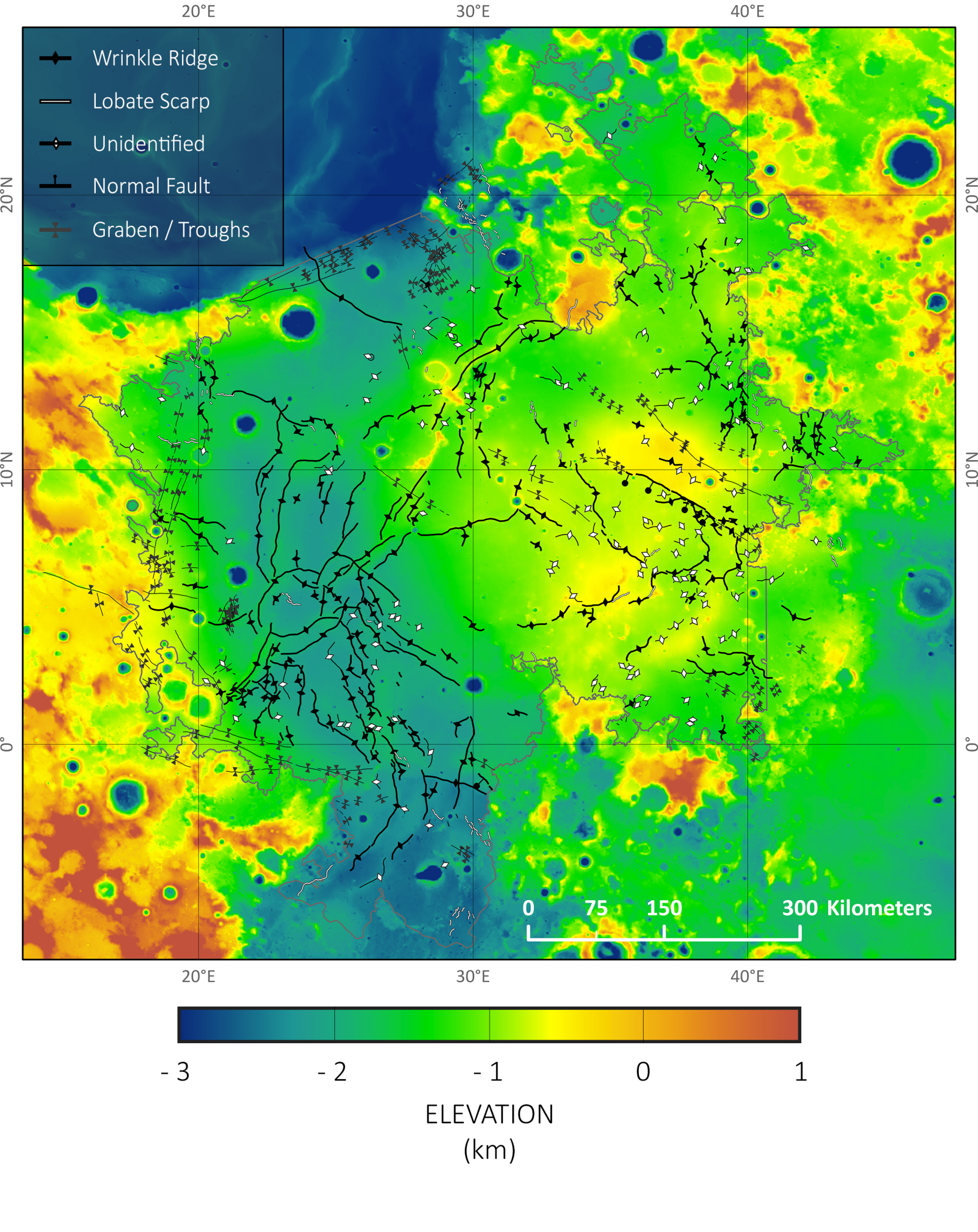
20°E
30°E
40°E
20°N
10°N
0°
Wrinkle Ridge
Lobate Scarp
Unidentified
Normal Fault
Graben / Troughs
0
75
150
300 Kilometers
- 3
- 2
- 1
0
1
ELEVATION
(km)

Figure 4.

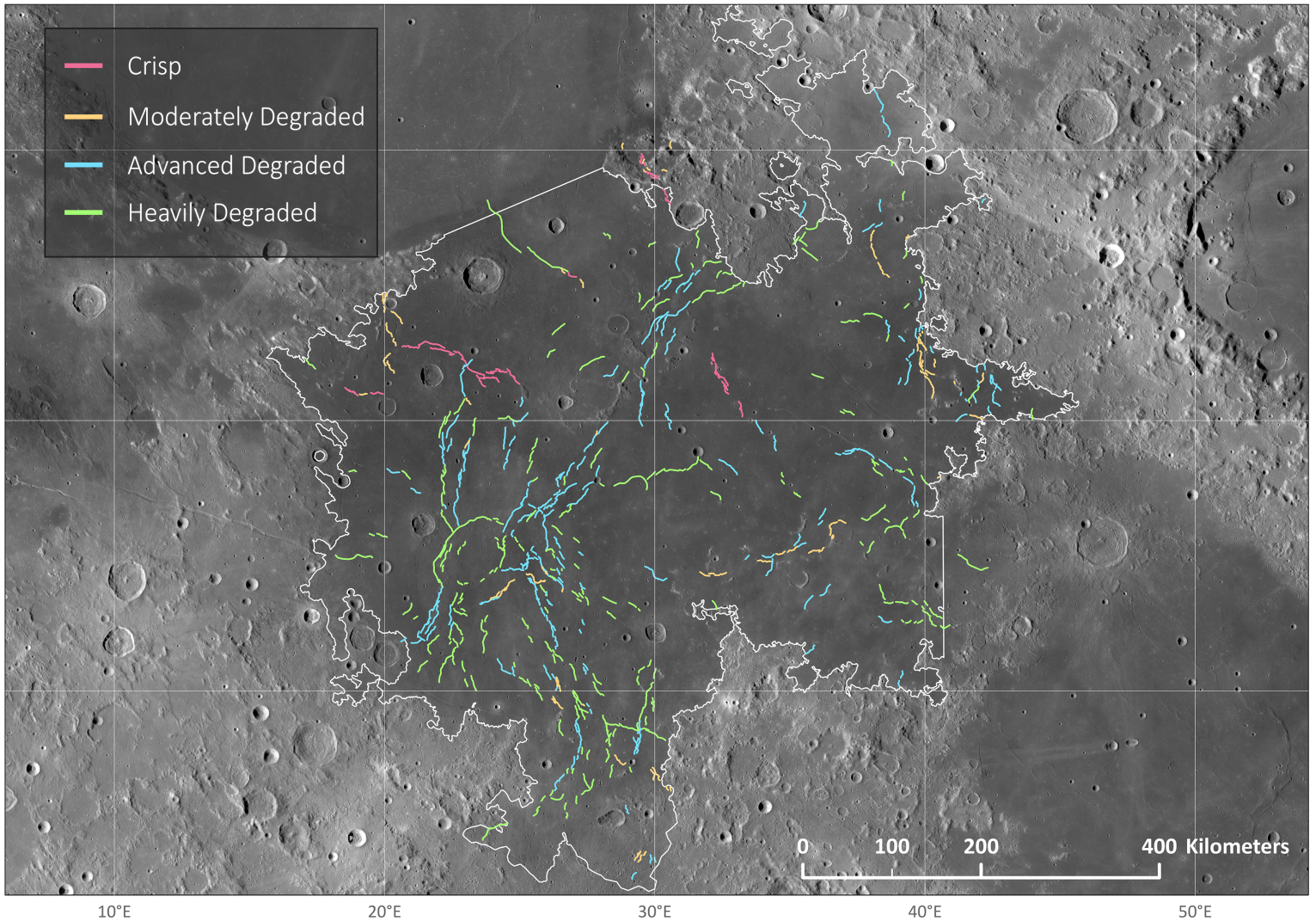
10°E
20°E
30°E
40°E
50°E
20°N
10°N
0°
Crisp
Moderately Degraded
Advanced Degraded
Heavily Degraded
0
100
200
400 Kilometers

Figure 5.

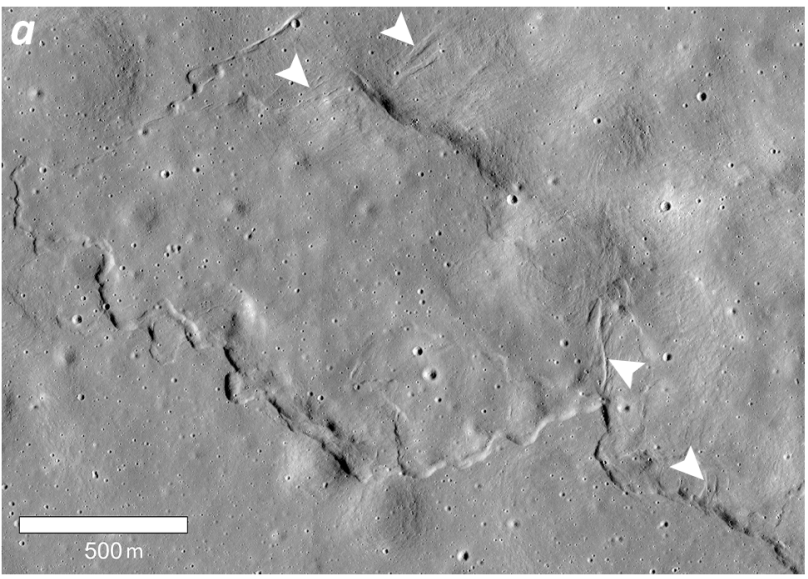
a
500 m

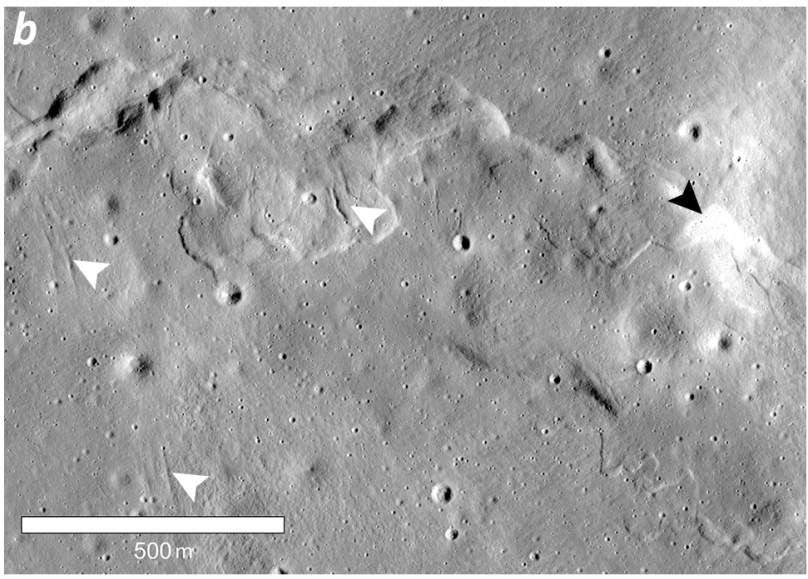
b
500 m

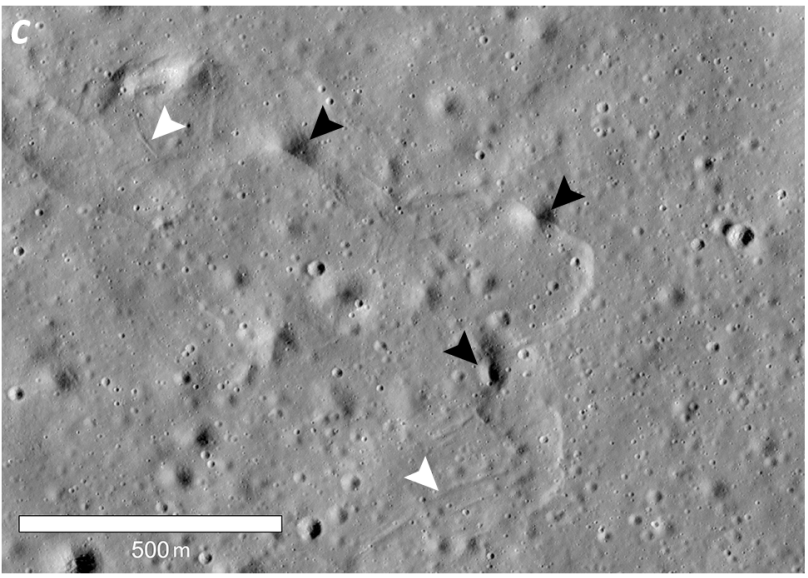
c
500 m

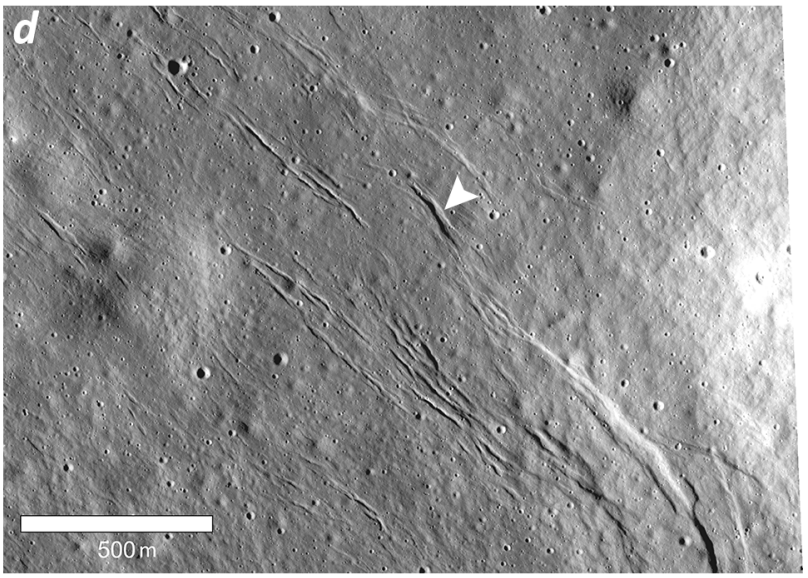
d
500 m

Figure 6.

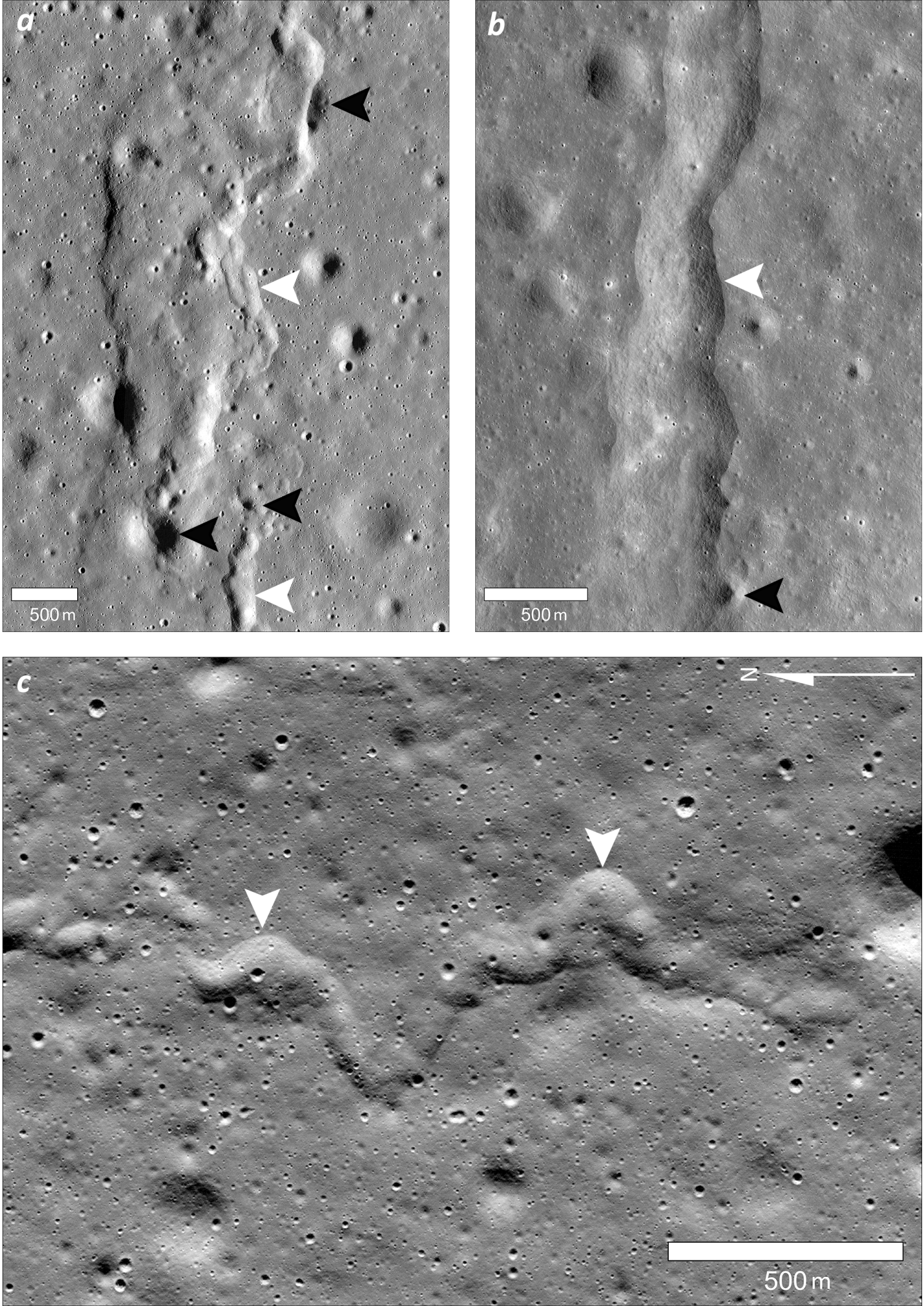
a
500 m
b
500 m
c
N
500 m

Figure 7.

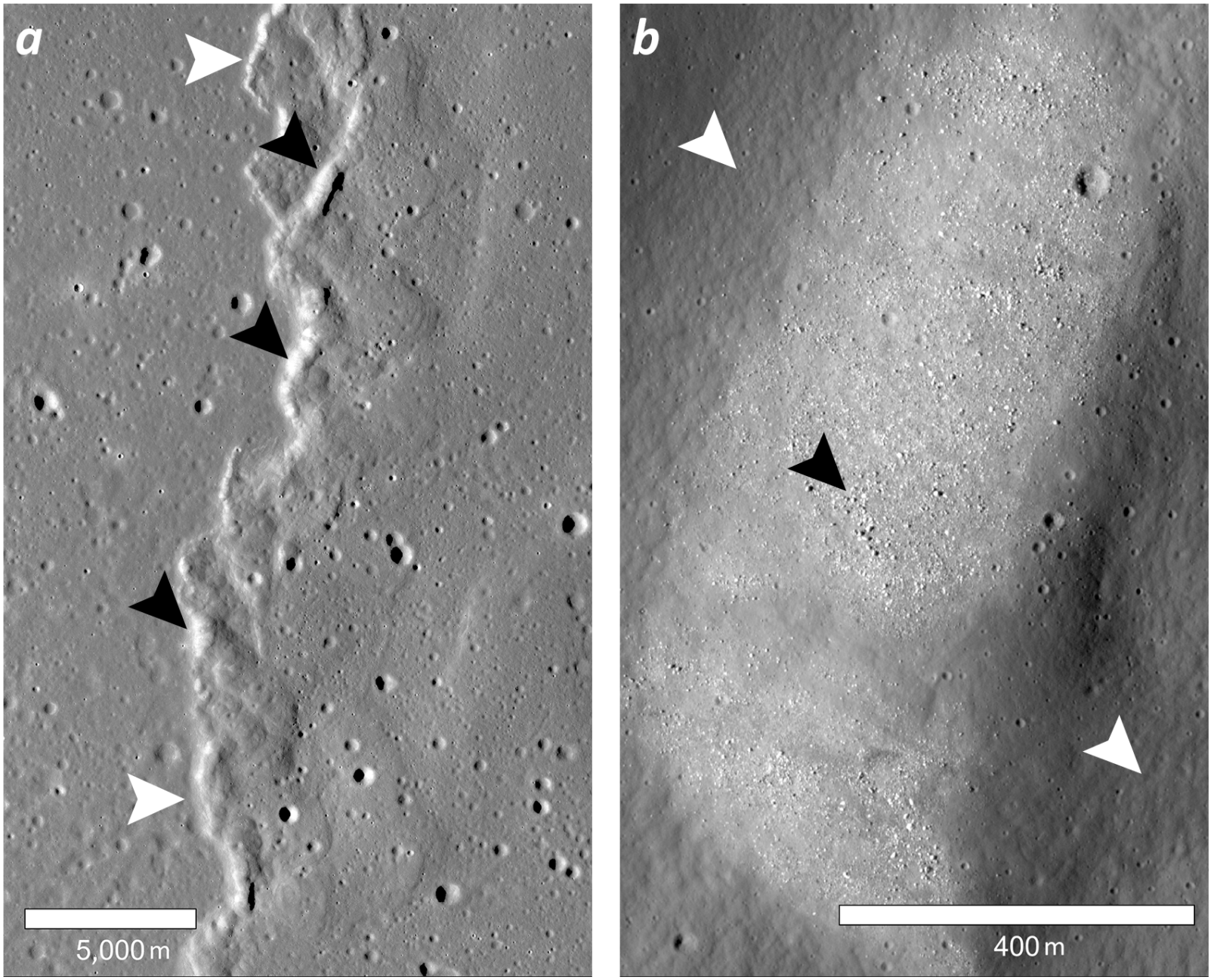
a
5,000 m
b
400 m

Figure 8.

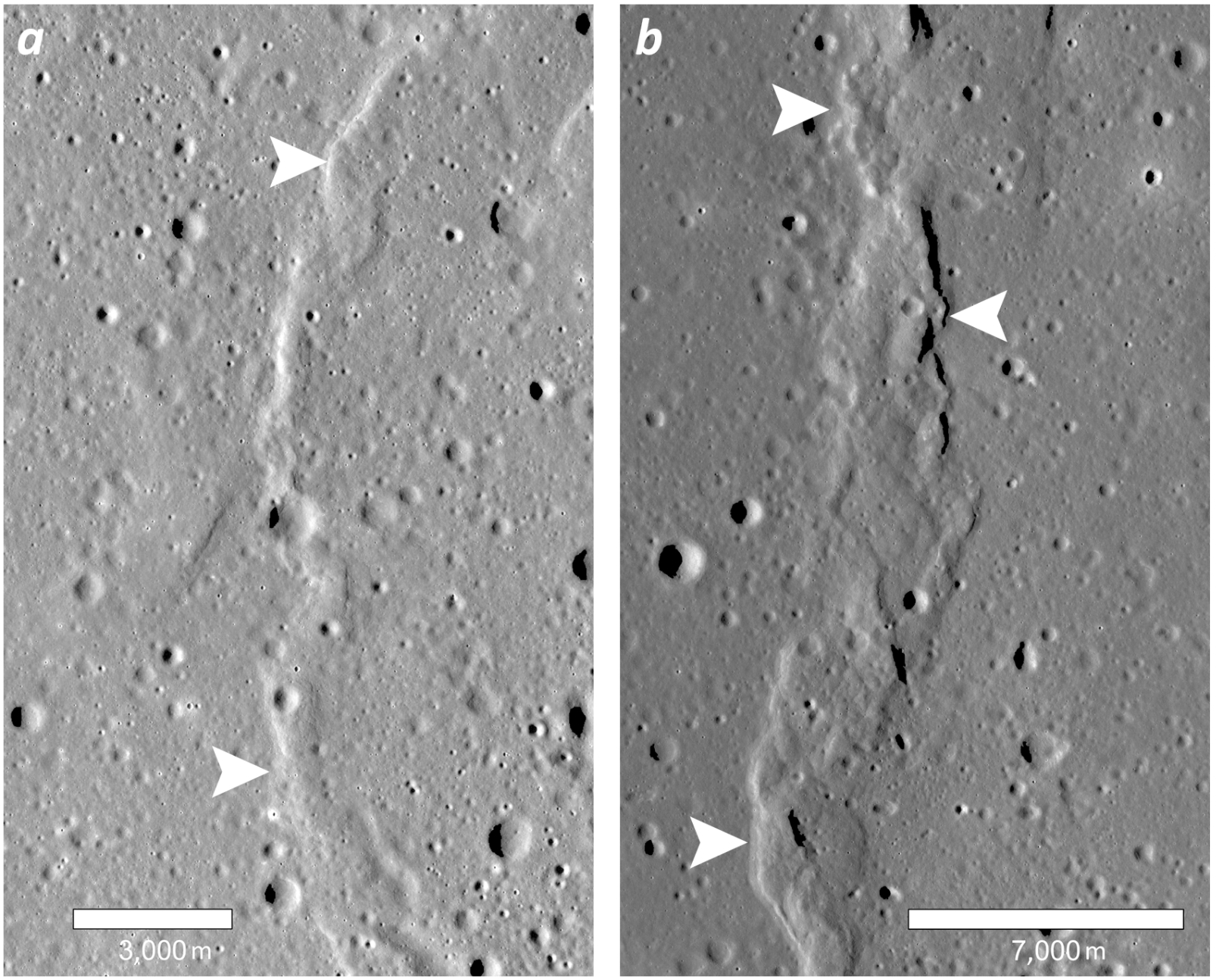
a
3,000 m
b
7,000 m

Figure 9.

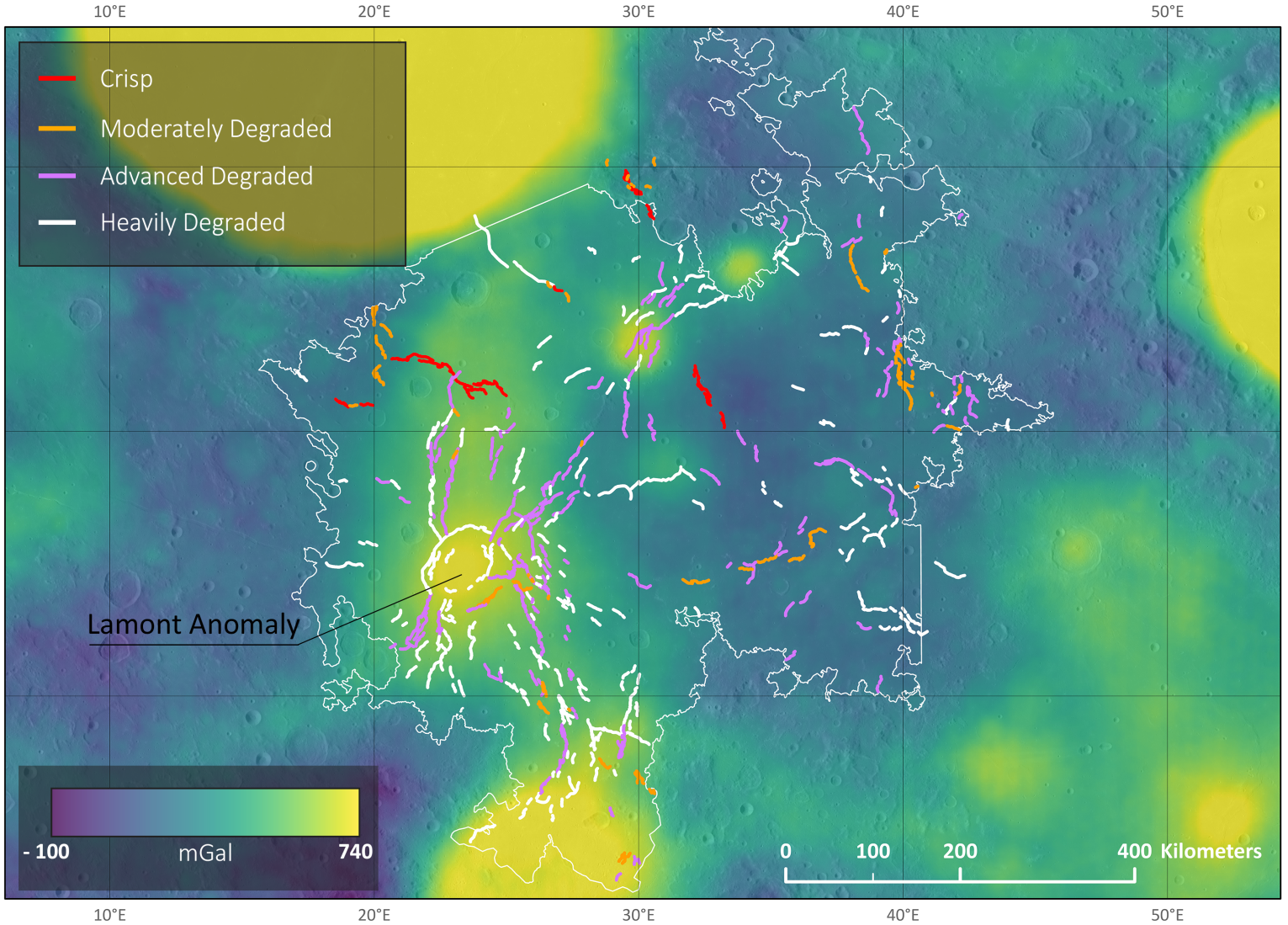
10°E
20°E
30°E
40°E
50°E
20°N
10°N
0°
Crisp
Moderately Degraded
Advanced Degraded
Heavily Degraded
Lamont Anomaly
- 100
mGal
740
0
100
200
400 Kilometers

Figure 10.

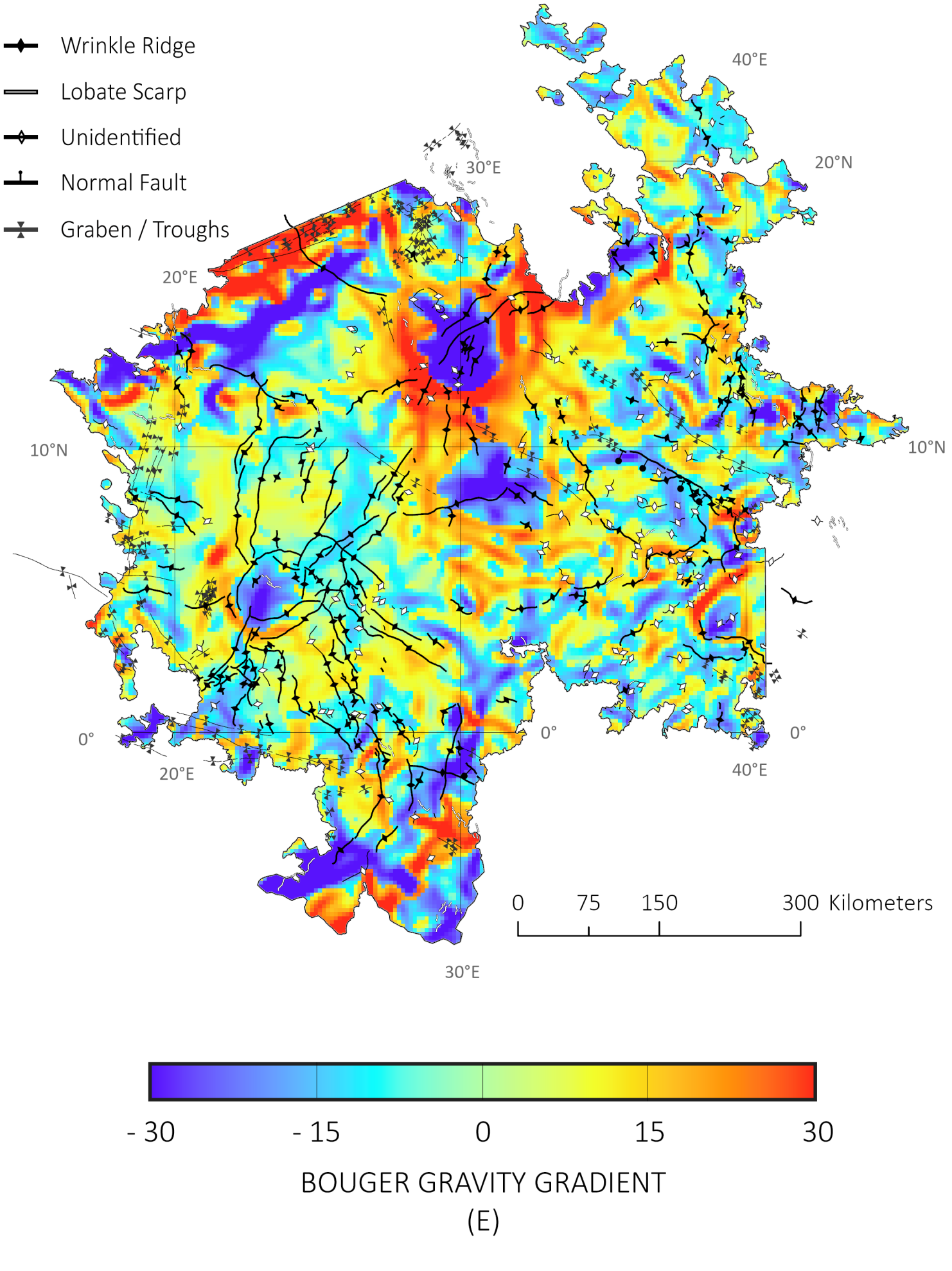
Wrinkle Ridge
Lobate Scarp
Unidentified
Normal Fault
Graben / Troughs
40°E
30°E
20°N
20°E
10°N
10°N
0°
0°
0°
20°E
40°E
30°E
0 75 150 300 Kilometers
- 30 - 15 0 15 30
BOUGER GRAVITY GRADIENT
(E)

Figure 11.

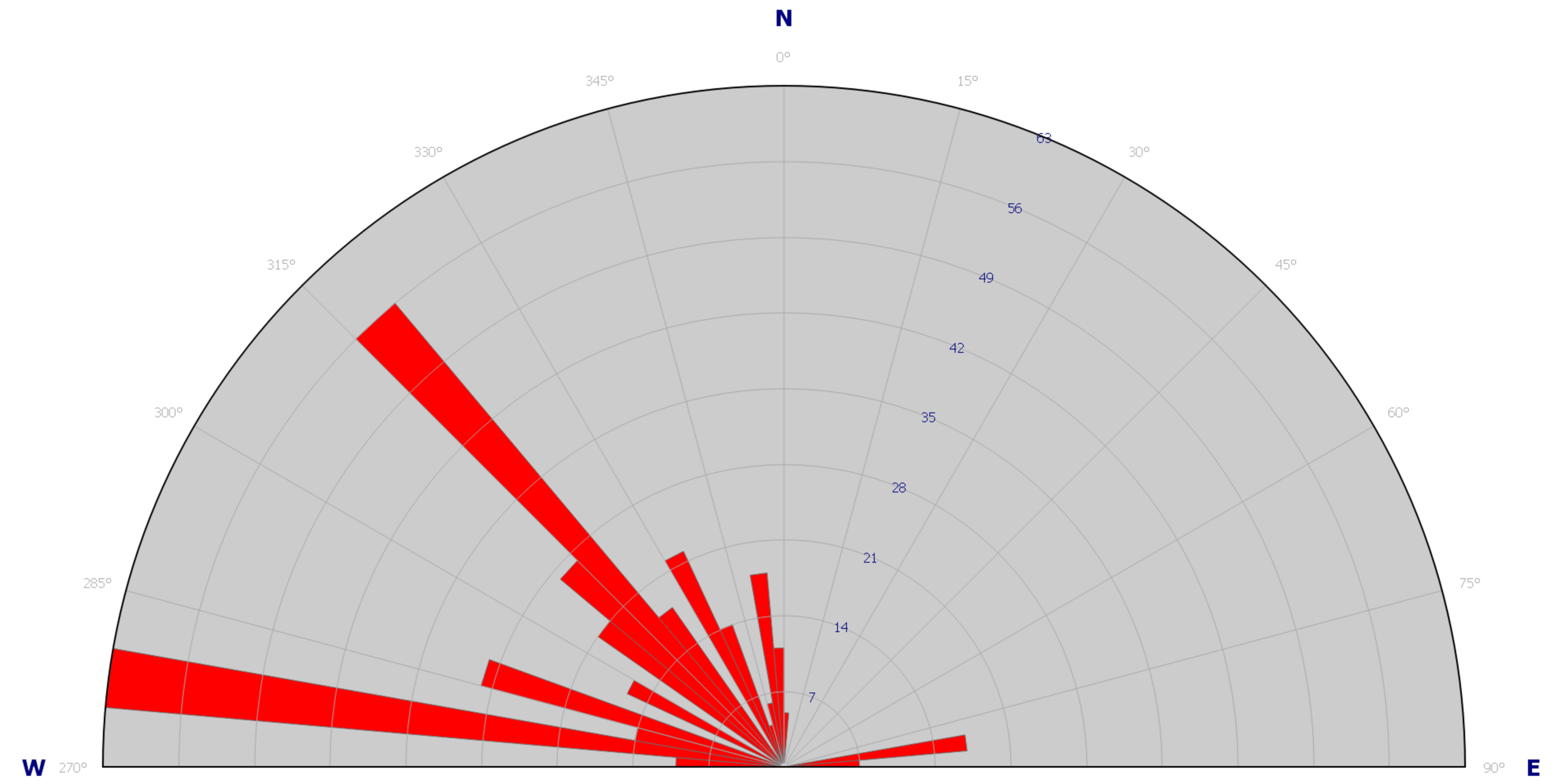
N
0°
345°
15°
330°
30°
315°
45°
300°
60°
285°
75°
270°
90°
W
E
63
56
49
42
35
28
21
14
7

Figure 12.

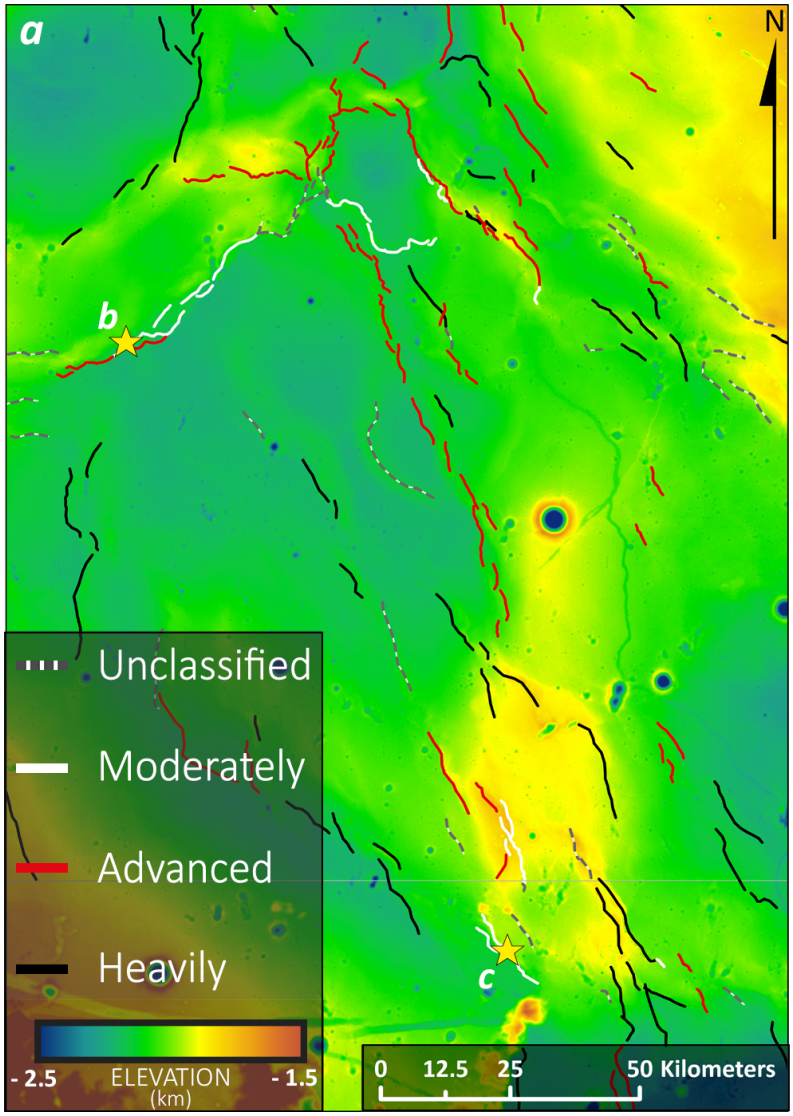
a
N
b
c
Unclassified
Moderately
Advanced
Heavily
- 2.5
ELEVATION
(km)
- 1.5
0
12.5
25
50 Kilometers

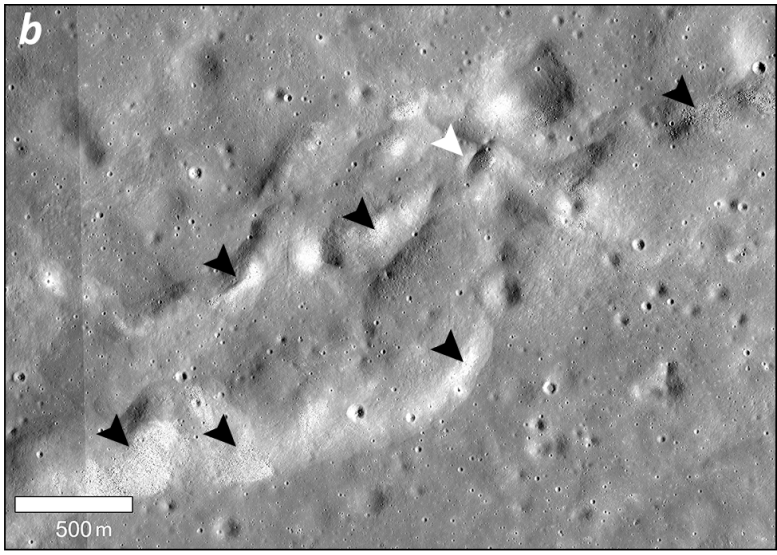
b
500 m

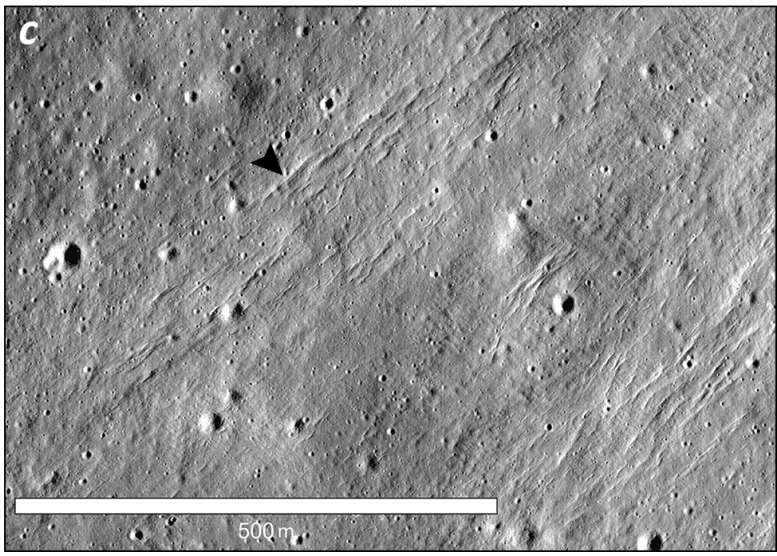
c
500 m

0°